Submesoscale Processes and Dynamics

Leif N. Thomas

Woods Hole Oceanographic Institution, Woods Hole, Massachusetts, USA

Amit Tandon

*Physics Department and Department of Estuarine and Ocean Sciences, University of Massachusetts, Dartmouth,
North Dartmouth, Massachusetts, USA*

Amala Mahadevan

Department of Earth Sciences, Boston University, Boston, Massachusetts, USA

Increased spatial resolution in recent observations and modeling has revealed a richness of structure and processes on lateral scales of a kilometer in the upper ocean. Processes at this scale, termed submesoscale, are distinguished by order-one ($O(1)$) Rossby and Richardson numbers; their dynamics are distinct from those of the largely quasi-geostrophic mesoscale as well as fully three-dimensional, small-scale processes. Submesoscale processes make an important contribution to the vertical flux of mass, buoyancy, and tracers in the upper ocean. They flux potential vorticity through the mixed layer, enhance communication between the pycnocline and surface, and play a crucial role in changing the upper-ocean stratification and mixed-layer structure on a timescale of days. In this review, we present a synthesis of upper-ocean submesoscale processes that arise in the presence of lateral buoyancy gradients. We describe their generation through frontogenesis, unforced instabilities, and forced motions due to buoyancy loss or down-front winds. Using the semi-geostrophic (SG) framework, we present physical arguments to help interpret several key aspects of submesoscale flows. These include the development of narrow elongated regions with $O(1)$ Rossby and Richardson numbers through frontogenesis, intense vertical velocities with a downward bias at these sites, and secondary circulations that redistribute buoyancy to stratify the mixed layer. We review some of the first parameterizations for submesoscale processes that attempt to capture their contribution to, first, vertical buoyancy fluxes and restratification by mixed-layer instabilities and, second, the exchange of potential vorticity between the wind- and buoyancy-forced surface mixed layer, and pycnocline. Submesoscale processes are emerging as vital for the transport of biogeochemical properties, for

generating spatial heterogeneity that is critical for biogeochemical processes and mixing, and for the transfer of energy from meso- to small scales. Several studies are in progress to model, measure, analyze, understand, and parameterize these motions.

1. INTRODUCTION

The oceanic mesoscale flow field, characterized by a horizontal length scale of 10 to 100 km, has been studied extensively for its dynamics and its contribution to the lateral transport of heat, momentum, and tracers by means of eddies. Similarly, three-dimensional processes at small lengthscales less than a kilometer (0.1–100 m) have been investigated for their contribution to mixing and energy dissipation. However, submesoscales (~1 km) that lie intermediate to meso- and small-scale three-dimensional motions are less understood and have only more recently been brought to light through observational, modeling, and analytical studies. The submesoscale, characterized by $\mathcal{O}(1)$ Rossby number dynamics, is not described appropriately by the traditional quasi-geostrophic theory that applies to mesoscales. It is not fully three-dimensional and nonhydrostatic, either, but is inevitably crucial to bridging the meso- and smaller scales through processes and dynamics that we are just beginning to understand. The objective of this article was to review and synthesize the understanding of submesoscales put forth through recent diverse studies.

Our discussion will focus on the upper ocean where submesoscale processes are particularly dominant due to the presence of lateral density gradients, vertical shear, weak stratification, a surface boundary that is conducive to frontogenesis, and a relatively small Rossby radius based on the mixed-layer depth. This is not to say that submesoscale phenomenon occurs solely in the upper ocean. In the ocean interior and abyss, there are submesoscale coherent vortices [*McWilliams*, 1985] and balanced flows associated with the oceanic vortical mode, which are thought to play an important role in the isopycnal stirring of tracers [*Kunze and Stanford*, 1993; *Kunze*, 2001; *Polzin and Ferrari*, 2003; *Sundermeyer and Lelong*, 2005]. Furthermore, internal gravity waves can vary on the submesoscale, but will not be described in this review.

The motivation to study submesoscale processes comes from several factors. As the geometrical aspect (depth to length) ratio and Rossby number Ro, associated with meso- and larger scale flow are $\ll 1$, and the Richardson number $Ri \gg 1$, the associated vertical velocities are 10^{-3} to 10^{-4} times smaller than the horizontal velocities, which are typically 0.1 m s^{-1}. However, localized submesoscale regions de-

velop in which Ro and Ri are $O(1)$. At these sites, submesoscale dynamics generate vertical velocities of $O(10^{-3})$ m s^{-1} or ~ 100 m day^{-1} that are typically an order of magnitude larger than those associated with the mesoscale. In addition, at the submesoscale, there is a marked asymmetry in the strength of upwelling versus downwelling and anticyclonic versus cyclonic vorticity, with an enhancement of downward velocity and cyclonic vorticity.

Owing to their large vertical velocities, submesoscale processes can be instrumental in transferring properties and tracers, vertically, between the surface ocean and the interior. This vertical transport plays an important role in supplying nutrients to the euphotic zone for phytoplankton production and exchanging gases between the atmosphere and the ocean. Understanding how vertical exchange is achieved between the biologically active, but nutrient-depleted, surface euphotic layer and the nutrient-replete thermocline has been a long-standing question for the carbon cycle and biogeochemistry of the upper ocean. For example, estimates of new production (phytoplankton production relying on a fresh rather than recycled supply of nutrients) based on oxygen utilization and cycling rates [*Platt and Harrison*, 1985; *Jenkins and Goldman*, 1985; *Emerson et al.*, 1997] and helium fluxes [*Jenkins*, 1988] are much higher in the subtropical gyres than can be accounted for through the physical circulation in global carbon cycle models [*Najjar et al.*, 1992; *Maier-Reimer*, 1993]. Several studies, such as those of *McGillicuddy and Robinson* [1997] and *McGillicuddy et al.* [1998], suggest that mesoscale eddies act to pump nutrients to the euphotic zone. However, a basinwide estimate for the eddy-pumping fluxes [*Oschlies*, 2002a; *Martin and Pondaven*, 2003; *Oschlies*, 2007] turns out to be inadequate in supplying the nutrient flux required to sustain the observed levels of productivity in the subtropical gyres. As described above, vertical velocities associated with submesoscale features are much stronger than their mesoscale counterparts, suggesting that submesoscale vertical fluxes of nutrients may play a critical role in enhancing productivity not only in the subtropical gyres but in the world ocean as a whole.

A large part of the ocean's kinetic energy resides at meso- and larger scales. At these scales, oceanic flow is largely two-dimensional and in a state of hydrostatic and geostrophic balance from which it is difficult to extract energy.

A major conundrum [*McWilliams et al.*, 2001; *McWilliams*, 2003], therefore, is how energy is transferred from the mesoscale to the small scale at which it can be dissipated through three-dimensional processes. The strong ageostrophic flow at submesoscales can extract energy from the balanced state and transfer it to smaller scales. *Charney* [1971] argued that large-scale stirring would induce a forward enstrophy cascade consistent with a kinetic energy spectrum of slope −3. For the oceanic context, numerical simulations have shown that the quasi two-dimensional mesoscale flow field is characterized by kinetic energy spectra with a slope of −3 [*Capet et al.*, 2008a; *Klein et al.*, 2007]. Three-dimensional numerical simulations at progressively finer resolutions show that resolving submesoscale processes leads to flattening the kinetic energy spectra slope to −2 [*Capet et al.*, 2008a] and a transfer of energy to larger as well as smaller scales [*Boccaletti et al.*, 2007].

Yet, another factor associated with submesoscale instabilities is the flux of potential vorticity to and from the surface to the interior ocean and the change in stratification of the mixed layer. Submesoscale instabilities in the mixed layer are shown to hasten restratification and buoyancy transport several-fold as compared to what can be achieved through mesoscale baroclinic instability [*Fox-Kemper et al.*, 2007]. Hence, their contribution to eddy transport can be significant. Present-day global circulation models do not resolve submesoscales; conceivably, this is the reason for the dearth of restratifying processes and mixed layers that are far too deep in the models [*Oschlies*, 2002b; *Hallberg*, 2003; *Fox-Kemper et al.*, 2007]. Hence, parameterizing these processes is of interest to climate modeling. Similarly, the cumulative vertical flux of potential vorticity through submesoscale processes can alter the potential vorticity budget of the thermocline and mixed layer [*Thomas*, 2005, 2007]. Submesoscale dynamics provide a pathway between the surface boundary layer, where properties are changed by friction and diabatic processes, and the interior, which is largely adiabatic and conserves properties.

Resolving submesoscales within the mesoscale field has been a challenge for models and observations, but one that is being currently met through improvements in technology. Hydrographic surveys using towed vehicles (such as a Sea-Soar) equipped with conductivity-temperature-depth sensors have revealed submesoscale features in the upper ocean associated with compensated and uncompensated ocean fronts [e.g., *Pollard and Regier*, 1992; *Rudnick and Luyten*, 1996; *Rudnick and Ferrari*, 1999; *Lee et al.*, 2006b]. Shipboard acoustic Doppler current profiler velocity measurements show that the distribution of the relative vorticity in the upper ocean is skewed to positive values, hinting at the presence of submesoscale flows with stronger cyclonic versus anticyclonic vorticity [*Rudnick*, 2001]. Recent observations centered around a drifter show the role played by the baroclinicity in setting the stratification within the mixed layer (Hosegood et al., Restratification of the surface mixed layer with submesoscale lateral gradients: Diagnosing the importance of the horizontal dimension, submitted to *Journal of Physical Oceanography*, 2007). Similar measurements made following mixed-layer Lagrangian floats have captured rapid (occurring over a day) changes in the mixed-layer stratification that cannot be ascribed to heating or cooling, and hence, are thought to result from submesoscale processes [*Lee et al.*, 2006a]. Further examples of submesoscale variability are seen in high-resolution velocity fields from radar [*Shay et al.*, 2003], sea-surface temperature fields from satellites [*Flament et al.*, 1985; *Capet et al.*, 2008b], a proliferation of cyclonic vortices revealed by sunglitter on the sea surface [*Munk et al.*, 2000], and biogeochemical sampling along ship transects. We are at an exciting juncture because we are now able to achieve the required resolution in models and observations to capture this scale. The results from high-resolution numerical modeling and analytical studies, several of which are discussed in this review, suggest that both forced and unforced instabilities drive submesoscale processes.

We begin section 2 by defining the term submesoscale and describing phenomena with which it is associated. Furthermore, we examine mechanisms that generate submesoscales in the upper ocean. In section 3, we present a mathematical framework for understanding the secondary circulation associated with fronts where submesoscale processes are found to be active. This framework is used to provide a dynamical explanation for several key features of submesoscale phenomena. In section 4, we discuss the implications of submesoscale phenomena, which include mixed-layer restratification, vertical transport and biogeochemical fluxes, and potential vorticity fluxes. Finally, we provide a discussion of outstanding questions and possible connections to other areas.

2. PHENOMENOLOGY

2.1. What are Submesoscales?

An active flow field in the upper ocean generates localized regions, typically along filaments or outcropping isopycnals, within which the relative vertical vorticity $\zeta = v_x - u_y$ equals or exceeds the planetary vorticity f, and the vertical shear can be quite strong. The dynamics within these regions differs from mesoscale dynamics characterized by small Rossby numbers ($Ro \ll 1$) and large Richardson numbers $(Ri \gg 1)$. We thus define submesoscale flows

based on dynamics, as those where the gradient Rossby number, $Ro = |\zeta|/f$, and the gradient Richardson number, $Ri = N^2/|\partial_z \mathbf{u}_h|^2$, are both $\mathcal{O}(1)$, where $\mathbf{u}_h$ is the horizontal velocity, $N^2 = b_z$ is the square of the buoyancy frequency, $b = -g\rho/\rho_o$ is the buoyancy, ρ is the density, g is the acceleration due to gravity, and ρ_o is a reference density. If we introduce bulk Richardson and Rossby numbers: $Ri_b = N^2H^2/U^2$ and $Ro_b = U/fL$ (U, H, and L are the characteristic speed, vertical lengthscale, and horizontal lengthscale of the velocity field, respectively), it then follows that submesoscale flows with $Ro_b = Ri_b = \mathcal{O}(1)$ are also characterized by an order-one Burger number $Bu = N^2H^2/f^2L^2$. It is worth noting that the bulk Richardson number can be related to the Froude number $Fr = U/NH = 1/\sqrt{Ri_b}$. Submesoscale flows, as we define them here, are hence characterized by $Fr \geq 1$. This parameter range with $Ro_b = \mathcal{O}(1)$ is also relevant to the transition from geostrophic to stratified turbulence [e.g., *Waite and Bartello*, 2006].

The characteristic vertical extent H of upper-ocean submesoscale phenomena typically scales with the mixed-layer depth h_{ml}. The condition that $Bu \sim 1$ implies that the horizontal lengthscale associated with submesoscale processes scales with the mixed-layer Rossby radius of deformation

$$L \sim L_{ml} = \frac{N_{ml}h_{ml}}{f}, \quad (1)$$

where N_{ml} is the buoyancy frequency in the mixed layer. The weak stratification and limited vertical extent of mixed layers makes the characteristic length of submesoscale flows small relative to the first baroclinic Rossby radius of deformation that defines the mesoscale. For example, a mixed layer of depth $h_{ml} = 100$ m, with $N_{ml} = 10^{-3}$ s^{-1} in the mid-latitudes ($f = 1 \times 10^{-4}$ s^{-1}), yields $L \sim L_{ml} = 1$ km. Given this small horizontal scale, it only takes a relatively weak velocity of $U = 0.1$ m s^{-1} to yield a Rossby number of order-one, indicating that such modest submesoscale flows can be susceptible to nonlinear dynamics and ageostrophic effects.

Another way to state the $Bu = 1$ condition is that the aspect ratio of submesoscale flows, $\Gamma = H/L$, scales as f/N. For typical oceanic conditions, $f/N \ll 1$, so that $\Gamma \ll 1$. Scaling the vertical momentum equation shows that the hydrostatic balance is accurate to $O(Ro^2\Gamma)$. Hence, although $Ro = \mathcal{O}(1)$ for submesoscale flows, $\Gamma \ll 1$ in the upper ocean, and these processes can, to a good approximation, be considered hydrostatic. Indeed, non-hydrostatic effects are difficult to detect in submesoscale model simulations at horizontal grid resolutions of 500 m [*Mahadevan*, 2006].

Another perspective used to understand submesocale processes is in terms of Ertel's potential vorticity (PV)

$$q = (f + \zeta)N^2 + \omega_h \cdot \nabla_h b, \quad (2)$$

where $\omega_h = (w_y - v_z, u_z - w_x)$ is the horizontal vorticity and $\nabla_h b$ is the horizontal buoyancy gradient. At large scales and in the interior, q is dominated by the planetary PV: fN^2. At mesoscales, the contribution from the vertical vorticity, ζN^2, becomes important. In the upper ocean, in the presence of density gradients arising from frontal filaments or outcropping isopycnals, the contribution to q from the horizontal buoyancy gradient and the thermal wind shear $(u_z^{tw}, v_z^{tw}) = (-b_y/f, b_x/f)$ becomes important and always tends to lower the PV. More specifically, the contribution to the PV from horizontal buoyancy gradients is as large as the planetary PV and significantly reduces the magnitude of the total PV when the Richardson number is $\mathcal{O}(1)$, that is, when the flow is submesoscale according to our dynamical definition [*Tandon and Garrett*, 1994; *Thomas*, 2007]. Submesoscale dynamics are thus intimately linked with processes that modify the PV, such as forcing by wind stress and buoyancy fluxes and advection of PV by eddies. This chapter therefore often uses PV as a means to help interpret submesoscale physics.

Next, we describe mechanisms that are known to be active in generating submesoscales including (1) frontogenesis; (2) unforced instabilities, such as the ageostrophic baroclinic instability [*Molemaker et al.*, 2005; *Boccaletti et al.*, 2007]; and (3) forced motion, such as flows affected by buoyancy fluxes or friction at boundaries. We will use the results from a numerical model to individually demonstrate the above submesoscale mechanisms. Although the submesoscale conditions are localized in space and time, the mesoscale flow field is crucial in generating them. In the ocean, it is likely that more than one submesoscale mechanism acts in tandem with mesoscale dynamics to produce a complex submesoscale structure within the fabric of the mesoscale flow field.

2.2. Frontogenesis

Consider the flow field generated by a geostrophically balanced front in the upper mixed layer of the ocean overlying a pycnocline. As the front becomes unstable and meanders, the nonlinear interaction of the lateral velocity shear and buoyancy gradient locally intensify the across-front buoyancy gradient. Strong frontogenetic action pinches outcropping isopycnals together, generating narrow regions in which the lateral shear and relative vorticity become very large, and the Ro and Ri become $\mathcal{O}(1)$. At these sites, the lateral strain rate $S \equiv ((u_x - v_y)^2 + (v_x - u_y)^2)^{1/2}$ is also large, and strong ageostrophic overturning circulation generates intense vertical velocities. In Figure 1, we plot the density, horizontal and vertical velocities, strain rate, Ro, and Ri from a frontal region in a model simulation. The model was initialized with an across-front density variation of 0.27 kg m^{-3}
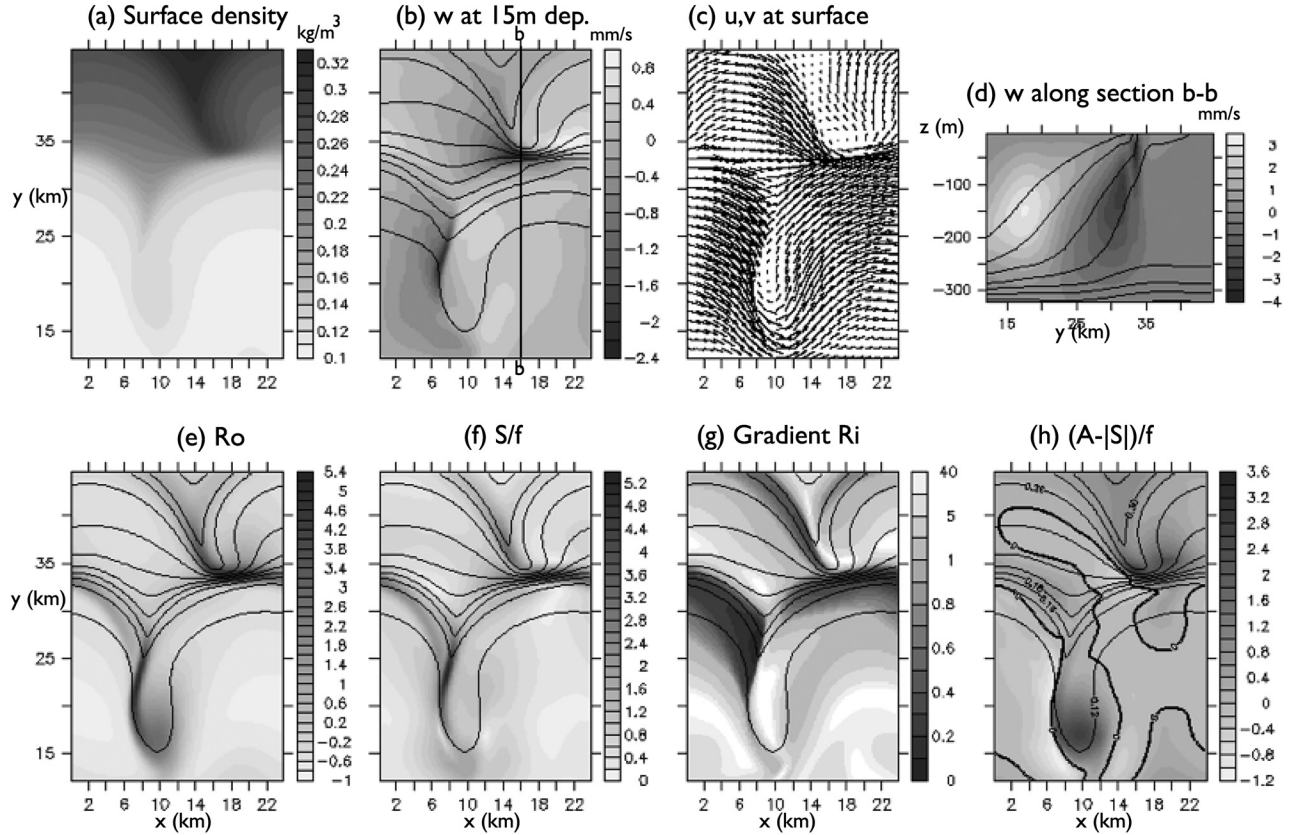
Figure 1. A region in the model domain where spontaneous frontogenesis has set up large shear and relative vorticity ζ, high lateral strain rate S, and a strong ageostrophic secondary circulation. (a) Surface density, (b) vertical velocity at 15 m depth, (c) surface u, v velocities, (d) vertical section through the front at $x = 16$ km showing vertical velocity (light tones indicate upward, dark tones downward) and isopycnals (black contours), (e) $Ro = \zeta/f$, (f) S/f, (g) gradient Ri, and (h) $(A - |S|)/f$ with the zero contour shown as a dark black line. Light black contours indicate surface density in all cases.

across 20 km (i.e., $|b_y| \approx 10^{-7}$ s^{-2}), over a deep mixed layer extending to 250 m and allowed to evolve in an east–west periodic channel with solid southern and northern boundaries. Submesoscale frontogenesis is more easily seen when the mixed layer is deep because the horizontal scale, which is dependent on h_{ml}, is larger and more readily resolved in the numerical model. Here, the mixed layer is taken to be 250 m deep so as to exaggerate frontogenesis. As the baroclinically unstable front meanders, the lateral buoyancy gradient is spontaneously locally intensified in certain regions, as in Figure 1, generating submesoscale conditions at sites approximately 5 km in width. This mechanism is ubiquitous to the upper ocean due to the presence of lateral buoyancy gradients and generates submesoscale phenomena when intensification can proceed without excessive frictional damping, or in a model with sufficient numerical resolution and minimal viscosity.

2.3. Unforced Instabilities

The instabilities in the mixed-layer regime where $Ro = \mathcal{O}(1)$ and $Ri = Ro^{-1/2} = \mathcal{O}(1)$ are different from the geostrophic baroclinic mode in several respects. The ageostrophic baroclinic instability problem of a sheared rotating stratified flow in thermal wind balance with a constant horizontal buoyancy gradient was investigated using hydrostatic [*Stone*, 1966, 1970] and non-hydrostatic equations [*Stone*, 1971] for finite values of Ro. *Molemaker et al.* [2005] extend these analyses by examining them in the context of loss of balance that leads to a forward energy cascade. Their instability analysis is applicable to the mixed-layer regime and shows two distinct instabilities. The largest growth rates arise for a geostrophic mode (large Ro Eady mode), which is mostly balanced and well captured by hydrostatic equations [*Stone*, 1966, 1970]. *Boccaletti et al.* [2007]

investigate an instability problem similar to *Molemaker et al.* [2005] and *Stone* [2007], although with a reduced gravity bottom boundary condition. They show that baroclinic instability arises at the mixed-layer Rossby radius of deformation, that is, (1), resulting in eddies of size $L = 1 - 10$ km in the mixed layer. While *Boccaletti et al.* [2007] call this instability ageostrophic (as the instability arises in a high *Ro* and small *Ri* regime), this mixed-layer instability (MLI) is the geostrophic mode of *Molemaker et al.* [2005] and is akin to the Eady mode for large *Ro*, small *Ri*. MLI, or the geostrophic mode, is mostly in balance (meaning that it can be diagnosed from PV), and its timescale, given by $Ri^{1/2}/f$, is $O(1/f)$, as $Ri \sim 1$. This timescale is much shorter than that of mesoscale baroclinic instability, and MLI hastens the slumping of fronts and hence leads to rapid restratification of the mixed layer.

In Figure 2, we show the evolution of the mixed-layer (balanced) mode or MLI in a model simulation as it rapidly restratifies the mixed layer. The model is initialized with a north-south buoyancy gradient in the mixed layer, which decays with depth in the upper thermocline. The east-west oriented front is seen to develop submesoscale meanders that merge and expand in lengthscale to the internal Rossby radius. As this occurs, lighter water overrides the denser side of the front, and as the frontal outcrop is pushed back, the front slumps and the mixed layer restratifies. The simulation replicates the phenomena in the work of *Boccaletti et al.* [2007]. In this unforced case, the submesoscale wiggles at the front grow at $\mathcal{O}(f^{-1})$ timescales between days 5 and 10 of the simulation, and transcend to mesoscale meanders within a couple of days by the upscale transfer of energy. The evolution of meanders then progresses at mesoscale timescales, but submesoscale processes continue to dominate the secondary circulation and the vertical fluxes at the front, leading to restratification. The values of the local *Ro* and gradient *Ri* during the evolution of the MLI suggest that the instability is largely driven by the ageostrophic component of the flow, although it is largely in gradient wind balance.
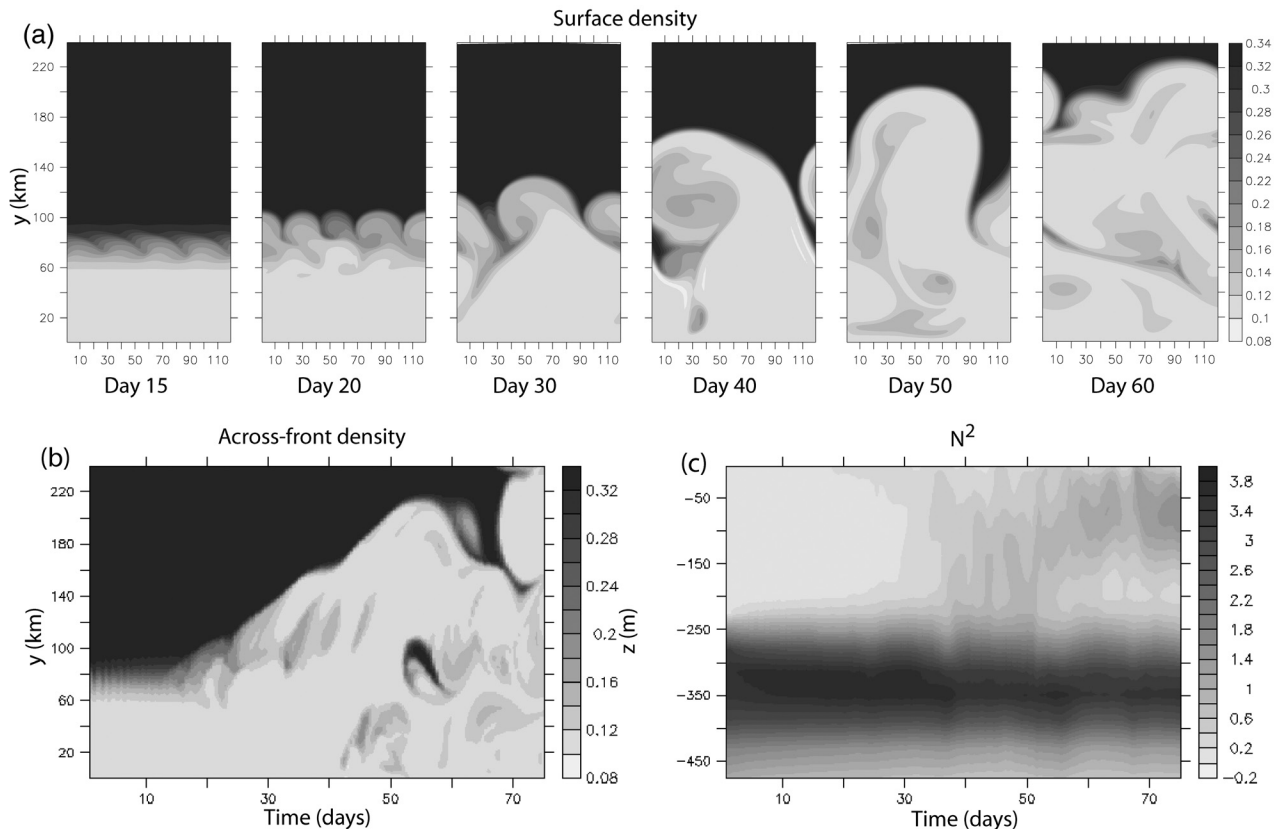
Figure 2. (a) Sequential figures of the surface density showing the evolution of the mixed layer instability. (b) Hovmöller plot of the across-front surface density at $x = 60$ km. (c) Hovmöller plot showing the evolution of the square of the buoyancy frequency N^2 over time averaged across the section at $x = 60$ km. The density is expressed in units of kg m^{-3}, while N^2 is multiplied by 10^5 and is expressed in s^{-2}.

A departure from balanced dynamics, in which submeso-scale dynamics most likely play an important role, facili-tates a forward cascade of energy [*McWilliams et al.*, 2001]. The nongeostrophic, unbalanced mode of *Molemaker et al.* [2005] requires that the difference between the absolute vorticity, $A = f + v_x - u_y$, and the magnitude of the strain rate, that is, $A - |S|$, changes sign. The frontal simulation in Figure 1 shows that this criteria is well satisfied in regions where active frontogenesis and MLI occur. However, diag-nosis of the unbalanced mode remains a challenge because a method is required to decompose the flow into its balanced and unbalanced components. The imbalance itself has to be characterized as either a departure from a hydrostatic and cyclostrophically adjusted state (pressure imbalance) or as a departure from a state that is fully diagnosable from the Ertel potential vorticity (PV imbalance). These different im-balance characterizations lead to different decompositions. PV-based decompositions for nonhydrostatic equations have been suggested by *McKiver and Dritschel* [2008] and *Viúdez and Dritschel* [2004]. In submesoscale-resolving numerical simulations, *Mahadevan and Tandon* [2006] used the quasi-geostrophic omega equation to diagnose the balanced verti-cal velocities and compared these to the vertical velocities from the three-dimensional model. Likewise, one may di-agnose the three-dimensional ageostrophic stream function (described in section 3.1.3) to represent the balanced flow and compare it with the ageostrophic secondary circulation (ASC) from the model. *Capet et al.* [2008a] calculate normal-ized departures from gradient wind balance in simulations of the California Current system. By successively increasing the horizontal model resolution, they see a greater depar-ture from gradient wind balance, indicative of unbalanced instabilities.

2.4. Forced Motions

Applying destabilizing atmospheric forcing to baroclinic mesoscale features can lead to the generation of submeso-scale motions. Destabilizing atmospheric forcing is defined as that which tends to reduce the stratification, Richardson number, and, more generally, the PV of the upper ocean. Such forcing can arise from heat or salt fluxes that extract buoyancy from the ocean or by down-front wind stress.

2.4.1. Buoyancy loss. Uniformly cooling a mesoscale flow or differentially cooling a laterally homogeneous layer can trigger submesoscale instabilities. The case of differential cooling was investigated by *Haine and Marshall* [1998] using non-hydrostatic numerical simulations run in two- and three-dimensional configurations. In both configurations, the differ-ential cooling creates a lateral buoyancy gradient that forms

a baroclinic jet through geostrophic adjustment. Due to the destabilizing forcing, the PV of the baroclinic jet is drawn to negative values, which, in the two-dimensional simulations, triggers symmetric instability of submesoscale ($\mathcal{O}(1$ km)) width that mixes the PV to create a mixed layer with nearly zero PV, nonzero stratification, and an order-one Richardson number. In the three-dimensional configuration, the jet goes unstable to baroclinic waves that have similar properties to the geostrophic mode described by *Molemaker et al.* [2005] and the MLI of *Boccaletti et al.* [2007], that is, with horizontal scales ~5 km and timescales of development of $\mathcal{O}(1$ day). The baroclinic instability of *Haine and Marshall* [1998] rapidly re-stratifies the mixed layer and grows in horizontal scale, as seen in the numerical experiments of *Boccaletti et al.* [2007] and the solution presented in Figure 2.

The case of uniform cooling of a mesoscale flow was in-vestigated using nonhydrostatic numerical simulations by *Legg et al.* [1998] and *Legg and McWilliams* [2001] for a flow consisting of an initial mesoscale eddy field and by *Yoshikawa et al.* [2001] for an ocean front. When a single cyclonic eddy is cooled by *Legg et al.* [1998], erosion of stratification reduces the Rossby radius of deformation to a value smaller than the radius of the eddy and allows for the formation of submesoscale baroclinic waves on the edges of the eddy. Numerical experiments in which a mixture of baroclinic cyclonic and anticyclonic eddies are cooled were analyzed by *Legg and McWilliams* [2001]. In these experi-ments, the barotropic eddy kinetic energy is observed to increase at a faster rate as compared to the case without cooling, suggesting that cooling, by triggering submesos-cale baroclinic instability, provides an additional means of converting available potential energy at mesoscales to baro-tropic eddy kinetic energy.

Yoshikawa et al. [2001] detailed the way in which desta-bilizing buoyancy fluxes at an ocean front can enhance the frontal vertical circulation. Comparing forced and unforced model runs, they showed that lateral strain associated with baroclinic instabilities was stronger for fronts forced by cool-ing and resulted in more intense frontogenesis. Using the semi-geostrophic omega equation, *Yoshikawa et al.* [2001] demonstrated that the amplified frontogenetic strain, com-bined with the cooling-induced low PV in the mixed layer, causes an enhancement in the strength of the frontal vertical circulation. We will elaborate on the dynamics of this impor-tant result in section 3.1.1.

2.4.2. Down-front wind stress. Down-front winds, that is, winds blowing in the direction of the surface frontal jet, re-duce the stratification and Richardson number in the surface boundary layer and thus provide favorable conditions for submesoscale phenomena [*Thomas and Lee*, 2005; *Thomas*,

2005]. Non-hydrostatic simulations show that for this wind orientation, Ekman flow advects denser water over light, destabilizing the water column and triggering convective mixing [*Thomas and Lee*, 2005]. The strength of this mixing is set by the magnitude of the surface lateral buoyancy gradient and the Ekman transport, the latter being a function of the vorticity of the flow. This is because flows with $\mathcal{O}(1)$ Rossby number exhibit nonlinear Ekman dynamics in which the advection of momentum plays a role in the Ekman balance. This causes the Ekman transport to vary inversely with the absolute, rather than planetary, vorticity [*Stern*, 1965; *Niiler*, 1969; *Thomas and Rhines*, 2002]. One of the more striking results of nonlinear Ekman dynamics is that a spatially uniform wind stress will induce Ekman pumping or suction if it is blowing over a current with lateral variations in its vorticity field. For example, a down-front wind blowing over a frontal jet will drive surface Ekman transport from the dense to light side of the front. The transport is weaker (stronger) on the cyclonic (anticyclonic) side of the jet and hence induces a secondary circulation with convergence and downwelling on the dense side of the front and divergence and upwelling at the center of the jet. Localized mixing caused by Ekman-driven convection at the front drives an additional secondary circulation. For down-front winds, frontal intensification can occur when the two secondary circulations modify the vertical vorticity and lateral buoyancy gradient in such a way as to enhance the nonlinear Ekman pumping or suction and Ekman-driven convection, thus reinforcing the secondary circulations themselves. This positive feedback mechanism can lead to the growth of multiple fronts in a mixed layer with an initially spatially uniform horizontal buoyancy gradient forced by down-front winds [*Thomas and Lee*, 2005].

The submesoscale-resolving, wind-forced model simulations of *Mahadevan and Tandon* [2006] and *Capet et al.* [2008a] show a preponderance of positive vorticity at submesoscales. Downward velocities are more intense and narrowly confined in elongated regions relative to upward velocities. The simulations of *Mahadevan and Tandon* [2006] demonstrate how even a weak, sustained downfront wind stress (of magnitude 0.025 N m^{-2}) generates a profusion of frontal structures that exhibit very large strain rates, relative vorticity, and vertical velocities in the surface mixed layer. These characteristics can be explained by SG dynamics, as shown in section 3.1.1. In contrast to the upper ocean, the velocity structure in the stratified pycnocline remains largely mesoscale in character.

Convective mixing induced by down-front winds leads to a reduction in the PV. This modification of the PV is due to an upward frictional PV flux that extracts PV from the ocean. The numerical simulations of *Thomas* [2005] demonstrate how this frictional PV flux is transmitted through the oceanic surface layer by submesoscale secondary circulations that downwell low PV from the surface while upwelling high PV from the pycnocline, yielding a vertical eddy PV flux that scales with the surface frictional PV flux. Although these numerical experiments were two-dimensional, fully three-dimensional simulations of wind-forced fronts have also shown such a vertical exchange of PV by submesoscale frontal circulations [*Capet et al.*, 2008b; *Mahadevan and Tandon*, 2006; *Thomas*, 2007]. In the work of *Thomas* [2007], the subduction of the low PV surface water results in the formation of a submesoscale coherent vortex or intrathermocline eddy. The vortex was shown to exert an along-isopycal eddy PV flux that scales with the wind-driven frictional PV flux at the surface. The eddy PV flux drove an eddy-induced transport or bolus velocity down the outcropping isopycal, which had an effect on the large-scale mean flow. The correspondence of the eddy and frictional PV fluxes in both the two- and three-dimensional simulations suggests that a possible approach for parameterizing wind-forced submesoscale phenomena is to use a parameterization scheme based on PV fluxes, a subject that will be discussed further in section 4.2.

3. SUBMESOSCALE DYNAMICS

The timescale of variability for submesoscale flows is often not very distinct from the period of near-inertial internal gravity waves, but unlike internal gravity waves, submesoscale flows are to a large extent balanced. This implies that submesoscale dynamics are determined by a single scalar field from which all other variables (density, horizontal and vertical velocity, etc.) can be determined using an invertibility principle [*McKiver and Dritschel*, 2008]. In the most familiar approximate forms of the equations governing balanced flows, there are two choices for the controlling scalar field: the horizontal streamfunction (e.g., the balanced equations of *Gent and McWilliams* [1983]) and the potential vorticity (e.g., the quasi- and semigeostrophic models of *Charney* [1948] and *Eliassen* [1948], respectively). Of the models listed above, the quasi-geostrophic (QG) model places the most severe restriction on the Rossby and Richardson numbers. QG theory assumes that $Ro \ll 1$ and $1/Ri \ll 1$; consequently, it is not designed to accurately describe the dynamics of submesoscale phenomena. A thorough study of the advantages and disadvantages of each model listed above can be found in *McWilliams and Gent* [1980]. In general, for flows with significant curvature, the balance equations are the most accurate [*Gent et al.*, 1994]. However, for relatively straight flows, the SG equations are accurate and provide insights into the dynamics of the intense fronts and vertical circulations typical of submesoscale features

in a relatively simple manner. In this section, we will describe some of the key features of submesoscale phenomena, namely frontogenesis, strong vertical circulation, restratification, forward cascade through frontogenesis, and nonlinear Ekman effects using the dynamical framework of the semigeostrophic equations.

3.1. Semigeostrophic Dynamics

In SG theory, the flow is decomposed into geostrophic and ageostrophic components $\mathbf{u} = \mathbf{u}_g + \mathbf{u}_{ag}$, where the geostrophic velocity $\mathbf{u}_g \equiv \hat{\mathbf{k}} \times \nabla_h p/f$ and p is the pressure. The SG equations are

$$\frac{D\mathbf{u}_g}{Dt} = -f\hat{\mathbf{k}} \times \mathbf{u}_{ag} \qquad (3)$$

$$0 = -\frac{1}{\rho_o}\frac{\partial p}{\partial z} + b \qquad (4)$$

$$\frac{Db}{Dt} = 0 \qquad (5)$$

$$\nabla \cdot \mathbf{u}_{ag} = 0, \qquad (6)$$

with $D/Dt = \partial/\partial t + (\mathbf{u}_g + \mathbf{u}_{ag}) \cdot \nabla$. These are valid if $D^2u/Dt^2 \ll f^2u$ and $D^2v/Dt^2 \ll f^2v$, that is, if the Lagrangian timescale of variability of the flow is much longer than an inertial period [*Hoskins*, 1975].

3.1.1. Two-dimensional vertical circulation. Consider a front in the $y - z$ plane, that is, $b_y \neq 0$ and $b_x = 0$ where the along-front velocity u is purely geostrophic, that is, $u = u_g$, and in thermal wind balance, $fu_{gz} = -b_y$. The two-dimensional ageostrophic circulation can be described by an across-front overturning streamfunction ψ where $(v_{ag}, w) = (\psi_z, -\psi_y)$. As first derived by *Eliassen* [1948] and *Sawyer* [1956], a single equation for ψ can be constructed by combining the y derivative of the buoyancy equation (5), with the z derivative of the zonal component of (3), yielding

$$F_2^2\frac{\partial^2\psi}{\partial z^2} + 2S_2^2\frac{\partial^2\psi}{\partial z\partial y} + N^2\frac{\partial^2\psi}{\partial y^2} = -2Q_2^g, \qquad (7)$$

where $N^2 = b_z$, $S_2^2 = -b_y = fu_{gz}$, $F_2^2 = f(f - u_{gy})$, and Q_2^g is the y component of the Q vector

$$\mathbf{Q}^g = (Q_1^g, Q_2^g) = \left(-\frac{\partial\mathbf{u}_g}{\partial x}\cdot\nabla b, -\frac{\partial\mathbf{u}_g}{\partial y}\cdot\nabla b\right) \qquad (8)$$

introduced by *Hoskins et al.* [1978]. A geostrophic flow with a nonzero Q vector will modify the magnitude of the horizontal buoyancy gradient following the equation

$$\frac{D}{Dt}|\nabla_h b|^2 = \mathbf{Q}^g \cdot \nabla_h b \qquad (9)$$

and will consequently disrupt the thermal wind balance of the flow. To restore geostrophy, an ASC is required, and its solution is governed by (7). The sign of the potential vorticity of the two-dimensional geostrophic flow

$$q_{2D} = \frac{1}{f}\left(F_2^2 N^2 - S_2^4\right) = fN^2\left[1 + Ro_{2D} - \frac{1}{Ri_{2D}}\right], \qquad (10)$$

where $Ro_{2D} = -u_{gy}/f$ and $Ri_{2D} = N^2/(u_{gz})^2$, determines the canonical form of (7). When $fq_{2D} > 0$, (7) is elliptic, but when $fq_{2D} < 0$, (7) is hyperbolic and has an entirely different character. Although (7) is formally valid only for two-dimensional ageostrophic motions, it is useful for diagnosing the importance of various mechanisms in generating an ASC and large vertical velocities in the presence of lateral buoyancy gradients. A three-dimensional version of this equation with diabatic and frictional effects is thus presented and discussed in section 3.1.3.

The solution to (7) can be found using the method of Green's functions. The Green's function for ψ satisfies the following equation:

$$F_2^2\frac{\partial^2 G}{\partial z^2} + 2S_2^2\frac{\partial^2 G}{\partial z\partial y} + N^2\frac{\partial^2 G}{\partial y^2} = \delta(y - \mathcal{Y}, z - \mathcal{Z}), \qquad (11)$$

which, for any Q−vector distribution yields the ageostrophic circulation: $\psi = -2\iint G(y - \mathcal{Y}, z - \mathcal{Z})Q_2^g(\mathcal{Y}, \mathcal{Z})d\mathcal{Y}d\mathcal{Z} + \psi_h$, where ψ_h is a homogeneous solution to (7) satisfying the boundary conditions. The solution to (11) for constant coefficients is

$$G = \frac{1}{4\pi\sqrt{fq_{2D}}}\log|\text{Arg}|, \qquad (12)$$

where

$$\text{Arg} = \frac{[(y - \mathcal{Y}) - (z - \mathcal{Z})S_2^2/F_2^2]^2}{L_{SG}^2} + \frac{(z - \mathcal{Z})^2}{H^2},$$
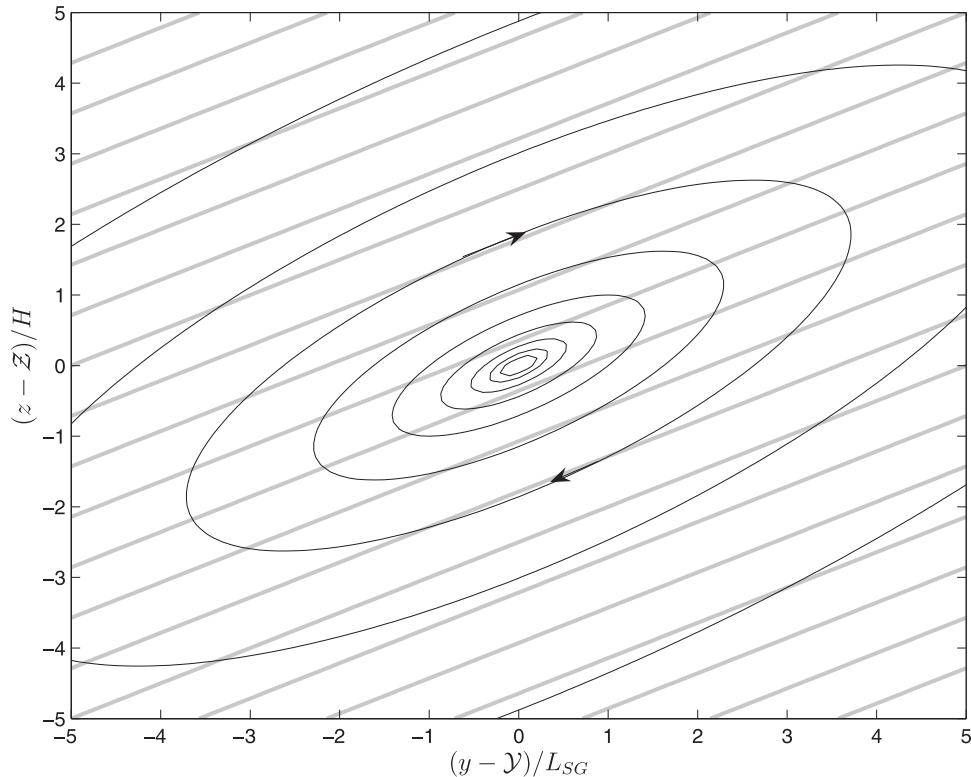
and

$$L_{SG} = H\frac{\sqrt{fq_{2D}}}{F_2^2} \qquad (13)$$

is the semigeostrophic Rossby radius of deformation and H is a characteristic vertical lengthscale of the flow [*Eliassen*, 1951; *Hakim and Keyser*, 2001]. G is plotted in Figure 3 for a buoyancy field that decreases in the y direction ($S_2^2 > 0$). Streamlines take the shape of tilted ellipses oriented at an angle $\theta = 0.5 \tan^{-1}[2S_2^2/(N^2 - F_2^2)]$. For typical conditions, $F_2^2 \ll |S_2^2| \ll N^2$, the ellipses are oriented parallel to isopycnals, $\tan\theta \approx S_2^2/N^2$, and the secondary circulations form slantwise motions along isopycnals. The sense of the secondary circulation of G is thermally direct, tending to flatten isopycnals. The Green's function is driven by a right-hand-side forcing of (7) corresponding to a negative point-source Q vector so that $\mathbf{Q}^g \cdot \nabla_h b > 0$, indicating that this secondary circulation is associated with frontogenetic forcing, that is, $D|\nabla_h b|^2/Dt > 0$. If either the buoyancy gradient or the direction of the Q vector were reversed, a thermally indirect circulation would be induced that tends to steepen isopycnals.

The vertical velocity associated with (12) is $-\partial G/\partial y$, or

$$w = -\frac{F_2^4}{2\pi(fq_{2D})^{3/2}H^2}\frac{(y - \mathcal{Y})}{\mathrm{Arg}} \tag{14}$$

and has a magnitude that varies greatly with the PV and vertical vorticity of the geostrophic flow. This solution suggests that for a given geostrophic forcing, in regions of low PV (where the Richardson number, stratification, or absolute vorticity of the fluid is small), the vertical circulation is strong. This amplification of the vertical circulation in regions of low PV was also noted by *Yoshikawa et al.* [2001], as noted in section 2.4.2. The solution given by (14) also suggests that w will be stronger in regions of cyclonic versus anticyclonic vorticity when both regions have the same PV. The enhancement of the vertical velocity in areas of low PV and high vertical vorticity is a consequence of the reduction in the characteristic horizontal lengthscale of the circulation in accordance with (13). This reduction in lengthscale is more pronounced for flows with high Rossby number and low Richardson number.
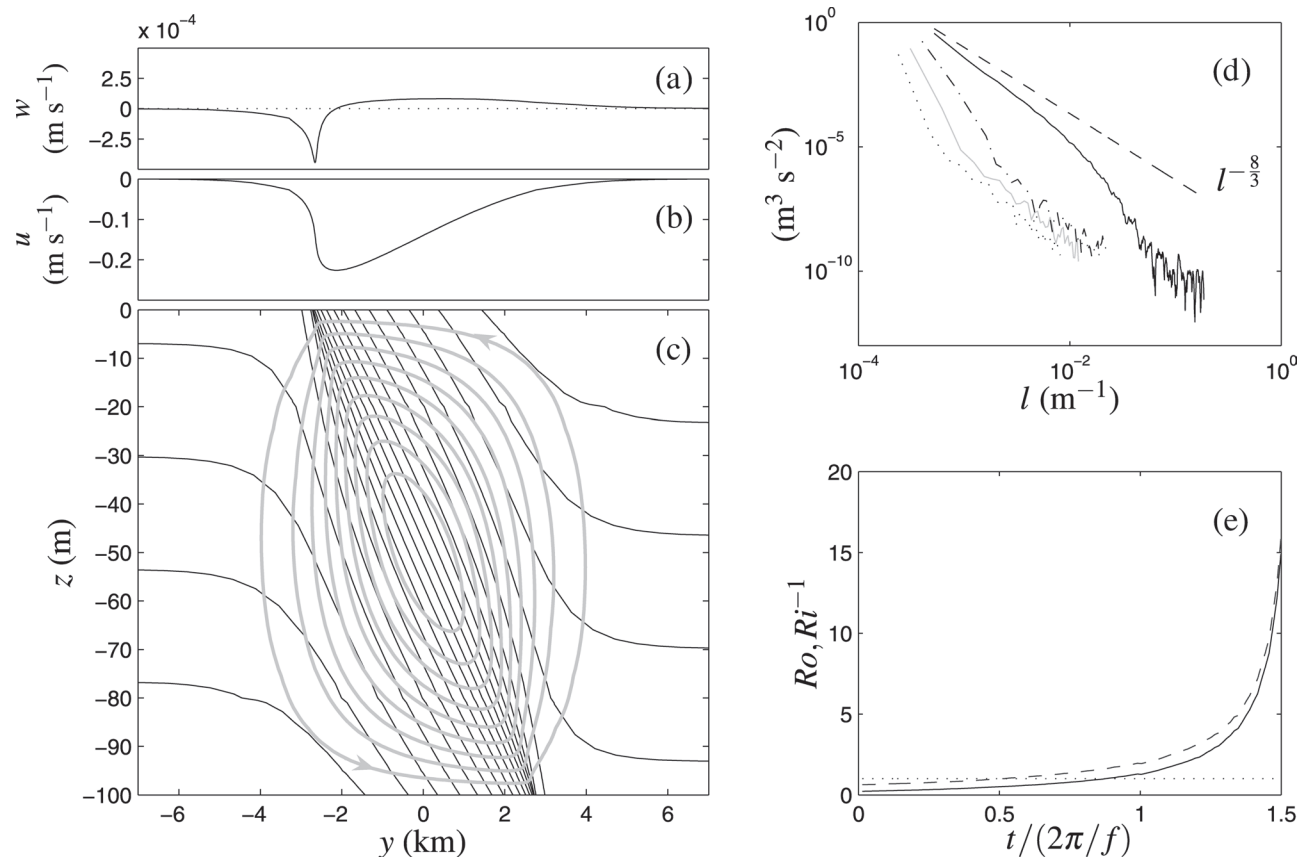
3.1.2. Horizontal deformation and frontal collapse. A simple yet dynamically insightful model for the formation of intense fronts in the submesoscale regime ($Ro \sim Ri \sim 1$) is the horizontal deformation model of *Hoskins and Bretherton* [1972]. In this model, the geostrophic flow is decomposed into two parts,

$$(u_g, v_g) = (\alpha x + u'_g(y, z, t), -\alpha y). \tag{15}$$

Figure 3. Ageostrophic secondary circulation G driven by a negative point-source Q vector, $Q_2^g < 0$, at $y = Y, z = Z$. Isopycnals (gray contours) slant upward to the north due to a southward buoyancy gradient. For this frontogenetic forcing, $\mathbf{Q}^g \cdot \nabla_h b > 0$, the circulation is thermally direct and tends to restratify the fluid.

The parts are associated with a deformation field with confluence α=constant>0, and a time-evolving, two-dimensional zonal flow u'_g, respectively. In the context of submesoscale phenomena, the deformation field could be associated with a mesoscale eddy field, while u'_g could be interpreted as an evolving submesoscale frontal feature. The equations are solved by introducing a geostrophic coordinate following the method of *Hoskins and Bretherton* [1972].

The solution for a front with an initial laterally varying buoyancy field $\mathcal{B} = \nabla b/2 \tanh(y/L)$, with $\Delta b = 0.0016$ m s^{-2} and $L = 4$ km, in a background stratification of $N_o^2 = 4.2 \times 10^{-6}$ s^{-2} and forced by a confluence $\alpha = 0.1f$ ($f = 1 \times 10^{-4}$ s^{-1}) is shown in Figure 4. As the geostrophic forcing is frontogenetic, a thermally direct secondary circulation with an upward vertical buoyancy flux $\overline{wb} > 0$ (the overline denotes a lateral average) is induced. The ageostrophic flow is itself frontogenetic and leads to the formation of a frontal discon-

tinuity in the zonal velocity and buoyancy field that first appears at the horizontal boundaries in a finite amount of time. During frontogenesis, asymmetric vertical vorticity and vertical velocity distributions are generated. Near the upper (lower) boundaries, regions of intense cyclonic vorticity and downward (upward) vertical velocities coincide, consistent with the argument presented in section 3.1.3 that the characteristic lateral lengthscale of the secondary circulation (13) is compressed in areas of high absolute vorticity. The formation of the discontinuity in the zonal velocity field causes the horizontal wavenumber spectrum of u to flatten in time, asymptoting to a $l^{-8/3}$ spectrum as the time of frontal collapse approaches [*Andrews and Hoskins*, 1978]. As the frontal discontinuity forms, the maximum in the Rossby and inverse Richardson numbers grows rapidly, taking on values greater than one. The evolution of Ro and Ri^{-1} closely track one another. This is a consequence of conservation of PV. For large

Figure 4. Solution of the horizontal deformation model for an initial buoyancy field $\mathcal{B} = \Delta b/2 \tanh(y/L)$: (a) w and (b) u at $z = -2.5$ m, and (c) the overturning streamfunction ψ (gray contours) and buoyancy b (black contours) at $t = 1.5$ inertial periods when frontal collapse at the boundaries is about to occur. (d) The horizontal spectrum of u at $z = 0$ for $t = 0.26$ (dotted), 0.67 (gray), 1.09 (dot–dash), and 1.50 (black) inertial periods. The dashed line denotes a −8/3 spectral slope. (e) Evolution of the maximum in the Rossby (solid) and inverse Richardson (dashed) number of the flow at $z = 0$. A dotted line at $Ro = Ri^{-1} = 1$ is plotted for reference.

Rossby numbers, the PV given by (10) is approximately $q_{2D} \approx fN^2(Ro_{2D} - Ri_{2D}^{-1})$ so that for the PV to be conserved, $Ro_{2D} \propto Ri_{2D}^{-1}$. Many of these features of the deformation model (asymmetric vorticity and w distributions, restratifying secondary circulations, flatter kinetic energy spectra, and coincident regions of high Rossby and low Richardson numbers) are typical of submesoscale flows and suggests that the simple physics encompassed in this model is quite relevant to the dynamics of submesoscale phenomena. It should be noted, however, that the semi-geostrophic equations can only be integrated until the first frontal discontinuity forms. Therefore, while semigeostrophic theory provides an accurate description of submesoscale frontal dynamics before frontal collapse, it cannot capture the continuing steepening of fronts after frontal collapse [*Boyd*, 1992].

3.1.3. Three-dimensional overturning circulation with frictional and diabatic effects. The semi-geostrophic equations can be used to study fully three-dimensional flows as well, provided that the cross-stream lengthscale is much less than the radius of curvature of the flow [*Gent et al.*, 1994]. In particular, semigeostrophic theory is useful for understanding the three-dimensional ageostrophic secondary circulation, which can concisely be described in terms of a vector streamfunction (ϕ, ψ) such that

$$u_{ag} = \frac{\partial \phi}{\partial z}, \quad v_{ag} = \frac{\partial \psi}{\partial z}, \quad w = -\left(\frac{\partial \phi}{\partial x} + \frac{\partial \psi}{\partial y}\right) \ (16)$$

[*Hoskins and Draghici*, 1977]. If friction or diabatic effects are included, then the governing equation for the ageostrophic circulation is

$$\begin{pmatrix} \mathcal{L}_{11} & \mathcal{L}_{12} \\ \mathcal{L}_{21} & \mathcal{L}_{22} \end{pmatrix} \begin{pmatrix} \phi \\ \psi \end{pmatrix} = \underbrace{-2\begin{pmatrix} Q_1^g \\ Q_2^g \end{pmatrix}}_{I} + \underbrace{f\frac{\partial}{\partial z}\begin{pmatrix} Y \\ -X \end{pmatrix}}_{II} - \underbrace{\begin{pmatrix} \frac{\partial \mathcal{D}}{\partial x} \\ \frac{\partial \mathcal{D}}{\partial y} \end{pmatrix}}_{III},$$

$$(17)$$

where (X,Y) are the components of the horizontal frictional force and $\mathcal{D}$ represents diabatic processes, that is,

$$\mathbf{F} = (X,Y) \quad \text{and} \quad \mathcal{D} \equiv \frac{Db}{Dt}. \quad (18)$$

For example, if lateral mixing of momentum and buoyancy are negligible, $(X,Y) = \partial_z(\tau^x, \tau^y)/\rho_o$ and $\mathcal{D} = -\partial_z F^B$, where (τ^x, τ^y) and F^B are the turbulent stress and vertical buoyancy flux, respectively. The differential operator on the left hand side of (17) is

$$\mathcal{L}_{11} = F_1^2 \partial_{zz} - 2S_1^2 \partial_{xz} + N^2 \partial_{xx}$$
$$\mathcal{L}_{12} = -C^2 \partial_{zz} + 2S_2^2 \partial_{xz} + N^2 \partial_{xy}$$
$$\mathcal{L}_{21} = -C^2 \partial_{zz} - 2S_1^2 \partial_{yz} + N^2 \partial_{xy}$$
$$\mathcal{L}_{22} = F_2^2 \partial_{zz} + 2S_2^2 \partial_{yz} + N^2 \partial_{yy},$$

where, N^2, F_2^2, and S_2^2 are the same as in (7), and the coefficients F_1^2, S_1^2, and C^2 are functions of the stratification, shear, and confluence or difluence of the geostrophic flow as follows:

$$F_1^2 = f\left(f + \frac{\partial v_g}{\partial x}\right), \ S_1^2 = f\frac{\partial v_g}{\partial z},$$
$$C^2 = -f\frac{\partial v_g}{\partial y} = f\frac{\partial u_g}{\partial x}. \quad (19)$$

As shown by *Hoskins and Draghici* [1977], equation (17) forced solely by the "geostrophic forcing" term I can be converted to the semigeostrophic omega equation.

Similar to the "geostrophic forcing", vertically varying frictional forces or laterally varying buoyancy sources or sinks (terms II and III respectively) will disrupt the thermal wind balance and hence drive ageostrophic circulations [*Eliassen*, 1951]. In addition, it is worth noticing that the equations governing nonlinear Ekman dynamics are encompassed in (17) when term II is balanced on the left hand side by terms with coefficients F_1^2 and F_2^2. For example, if the geostrophic flow were purely zonal and forced by a zonal wind stress τ_w^x, then the meridional Ekman transport $M_e^y = \int_{-\infty}^0 vdz$ can be found by vertically integrating term II twice and dividing by F_2^2 (assuming that u_g is approximately constant through the thickness of the Ekman layer) yielding

$$M_e^y = -\frac{\tau_w^x}{\rho_o(f - \partial u_g/\partial y|_{z=0})}, \quad (20)$$

which is the solution of *Stern* [1965] and *Niiler* [1969] alluded to in section 2.4.2. Term III is important at wind-forced fronts where Ekman flow can advect dense water over light, generating convection and turbulent mixing of buoyancy at the front. The strength of this mixing is set by a wind-driven buoyancy flux

$$F_{wind}^B = \mathbf{M}_e \cdot \nabla_h b|_{z=0}, \quad (21)$$

which is a function of both the lateral buoyancy gradient and, as a result of (20), the vertical vorticity of the front. This

mixing drives (through term III) frontogenetic ageostrophic secondary circulations [*Thomas and Lee*, 2005].

For submesoscale flows in the upper ocean, all three forcing terms of (17) are likely to play a role in driving an overturning circulation. In inferring the vertical velocities from high-resolution hydrographic and velocity observations in the upper ocean, it is often assumed that term I dominates the dynamics (i.e., the vertical velocity follows the omega equation) and that the ASC is well described by the quasi-geostrophic version of (17), that is with $F_1^2 \to f^2$, $F_2^2 \to f^2$, $C^2 \to 0$, $N^2 \to N^2$, $S_1^2 \to 0$, and $S_2^2 \to 0$ [e.g., *Pollard and Regier*, 1992; *Viúdez et al.*, 1996; *Rudnick*, 1996; *Allen and Smeed*, 1996; *Pinot et al.*, 1996; *Shearman et al.*, 1999; *Vélez-Belchí et al.*, 2005]. The validity of these assumptions comes into question for submesoscale flows, especially if the flows are exposed to atmospheric forcing. The QG omega equation does not work well for diagnosing vertical velocities when tested with a high-resolution numerical simulation that generates $\mathcal{O}(1)Ro$, as it misdiagnoses the position and sign of the most intense vertical velocities near the surface [*Mahadevan and Tandon*, 2006]. To account for departures from QG dynamics for high Rossby number flows, methods for diagnosing the vertical velocity from observations have been employed that use the inviscid, adiabatic semigeostrophic omega equation [*Naveira Garabato et al.*, 2001] or the generalized omega equation [*Pallàs Sanz and Viúdez*, 2005]. For forced upper ocean flows where friction and diabatic processes can be important, methods for inferring the overturning circulation using variants of (17) have been utilized [e.g., *Nagai et al.*, 2006; L. N. Thomas, C. M. Lee, and Y. Yoshikawa, The subpolar front of the Japan/East Sea II: Inverse method for determinig the frontal vertical circulation, submitted to *Journal of Physical Oceanography*, 2008].

To yield a unique solution for the ASC for given boundary conditions, (17) must be elliptic. Equation (17) switches from being elliptic to hyperbolic, and the semigeostrophic limit of balance is crossed when the three-dimensional semigeostrophic PV

$$q_{3D} = \left[\left(F_1^2 F_2^2 - C^4 \right) N^2 + 2C^2 S_1^2 S_2^2 - F_2^2 S_1^4 - F_1^2 S_2^4 \right] / f^3$$

(22)

multiplied by the Coriolis parameter becomes negative, that is $fq_{3D} < 0$. *Hoskins* [1975] demonstrated that the semigeostrophic equations without friction and diabatic terms, that is (3)–(6), can be manipulated to form a conservation law for q_{3D}, $Dq_{3D}/Dt = 0$. Although q_{3D} is materially conserved in an inviscid adiabatic fluid similar to the Ertel PV given by (2), it differs conceptually from q in that its conservation depends on the approximations used in semigeostrophic theory [*Viúdez*, 2005]. Having said this, the material invariance of (22) is consequential, as it im-

plies that in an adiabatic inviscid geostrophic flow that initially has $fq_{3D} > 0$ everywhere, the semigeostrophic equations can be integrated forward for all times, as the semigeostrophic limit of balance can never be crossed. When friction or diabatic effects are present, this is not always the case, as both q_{3D} and the Ertel PV (2) can be driven to negative values under certain conditions, as described in the next section. In three-dimensional numerical simulations [e.g., *Mahadevan and Tandon*, 2006], the regions where the PV changes sign tend to coincide with the sites of most intense submesoscale activity and downwelling.

3.2. Frictional or Diabatic Modification of the Potential Vorticity

Changes in the PV arise from convergences or divergences of PV fluxes

$$\frac{\partial q}{\partial t} = -\nabla \cdot \left(\mathbf{u}q + \mathbf{J}^{na} \right),$$

(23)

where q is the Ertel PV given by (2) and

$$\mathbf{J}^{na} = \nabla b \times \mathbf{F} - \mathcal{D}(f\hat{k} + \nabla \times \mathbf{u})$$

(24)

is the nonadvective PV flux [*Marshall and Nurser*, 1992]. *Thomas* [2005] shows that friction or diabatic processes, that is (18), acting at the sea surface will result in a reduction of the PV when

$$fJ_z^{na} = f \left[\nabla_h b \times \mathbf{F} \cdot \hat{k} - \mathcal{D}(f + \zeta) \right]\big|_{z=0} > 0.$$

(25)

Destabilizing atmospheric buoyancy fluxes reduce the buoyancy in the upper ocean $\mathcal{D} = Db/Dt < 0$, which, for inertially stable flows, $f(f + \zeta) > 0$, results in a diabatic PV flux that satisfies condition specified by (25) and reduces the PV. Friction can either input or extract PV from the fluid depending on the orientation of the frictional force and the lateral buoyancy gradient. Down-front winds drive PV fluxes that meet the condition specified by (25) and, as illustrated in nonhydrostatic simulations, Ekman-driven convection ensues to mix the stratification and reduce the PV [*Thomas and Lee*, 2005]. Friction injects PV into the fluid when a baroclinic current is forced by upfront winds or during frictional spindown by vertical mixing of momentum [*Boccaletti et al.*, 2007; (L. N. Thomas and R. Ferrari, Friction, frontogenesis and the stratification of the surface mixed layer, submitted to *Journal of Physical Oceanography*, 2007)]. Regardless of whether friction increases or decreases the PV, frictional modification of PV at the sea surface is largest in regions with strong lateral buoyancy gradients. Consequently, submesoscale phenomena with their enhanced baroclinicity are especially prone to frictional PV change.

4. IMPLICATIONS

As highlighted in the previous section, in the submeso-scale regime $Ro \sim Ri \sim 1$, vertical motions are enhanced. In this section, we discuss implications of the submesoscale vertical fluxes on budgets of the buoyancy, PV, and biogeochemical properties along with possible approaches to parameterization.

4.1. Effect on Mixed-Layer Stratification

The MLI described in section 2.3 release available potential energy from upper ocean fronts by inducing an upward buoyancy flux $\overline{w'b'}$ that tends to restratify the mixed layer, for example, Figure 2c. Submesoscale vertical buoyancy fluxes play an important role in the buoyancy budget of the mixed layer by competing with, or augmenting, buoyancy fluxes associated with small-scale turbulent motions. This may be expressed as

$$\partial_t \overline{b} + \nabla_h \cdot \left(\overline{\mathbf{u}'_h b'} + \overline{\mathbf{u}}_h \overline{b} \right) + \partial_z \left(\overline{w'b'} + \overline{w}\,\overline{b} \right) = \overline{\mathcal{D}}, \qquad (26)$$

where the overline denotes a lateral average, primes denote the deviation from that average, and the turbulent effects are encompassed in the diabatic term $\overline{\mathcal{D}}$. The horizontal and vertical eddy fluxes of buoyancy on the left-hand side of (26) have contributions from both mesoscale and submeso-scale flows. Submesoscale-resolving numerical experiments show that the vertical buoyancy flux $\overline{w'b'}$ is dominated by submesoscale eddies, while the lateral eddy buoyancy flux $\overline{\mathbf{u}'_h b'}$ is largely mesoscale [*Capet et al.*, 2008a; *Fox-Kemper et al.*, 2007]. While $\overline{w'b'}$ acts to redistribute buoyancy rather than generate a net input of buoyancy (as would be induced by an actual surface heat flux), expressing the vertical buoy-ancy flux in units of a heat flux gives the reader an apprecia-tion for the strong restratifying capacity of submesoscale flows and motivates a parameterization. The submesoscale vertical buoyancy fluxes simulated in the numerical experi-ments of *Capet et al.* [2008a] had values equivalent to heat fluxes of $\mathcal{O}$ (100 W m^{-2}). However, *Capet et al.* [2008a] find that in their forced model simulations, the sea surface temperature is not very sensitive to increasing grid resolu-tion because the increase in restratifying submesoscale ver-tical buoyancy fluxes, although significant, is offset by an equivalent change in $\overline{\mathcal{D}}$ that tends to destratify the mixed layer.

Fox-Kemper et al. [2007] propose parameterizing the submesoscale vertical buoyancy flux using an overturning streamfunction, that is $\overline{w'b'} = \Psi \overline{b}_y$ (y indicates the cross-front direction). Using both dynamical and scaling arguments, they suggest that Ψ takes the form

$$\Psi = C_e \mu(z) \frac{H^2 \overline{\overline{b}_y}^{\,z}}{|f|}, \qquad (27)$$

where H is the mixed layer depth and $\overline{\overline{b}_y}^{\,z}$ is the highest reso-lution cross-front buoyancy gradient in a non-submesoscale permitting simulation vertically averaged over the mixed layer. In performing a suite of numerical experiments with varying H, f, and lateral buoyancy gradients, some forced by a diurnally varying heat flux, but none by wind stress, *Fox-Kemper et al.* [2007] showed that the buoyancy fluxes predicted by (27) compare well with those of the numerical solutions when the constant C_e is in the range of 0.04 to 0.06 and the vertical structure function is $\mu(z) = -4z(z + H)/H^2$. Owing to its strong dependence on H, implementation of (27) in a global circulation model has the greatest impact in regions with deep mixed layers and is found to alleviate the problem of overly deep mixed layers at high latitudes (B. Fox-Kemper, personal communication, 2007).

### 4.2. Frictionally Driven Eddy Potential Vorticity Fluxes

As described in section 2.4.2, down-front, wind-forced baroclinic flows form submesoscale circulations that advect PV and induce eddy PV fluxes. In two-dimensional simula-tions, submesoscale ASCs drive vertical PV fluxes that scale with the surface frictional PV flux, i.e.,

$$\overline{w'q'} \propto \overline{\nabla_h b \times \mathbf{F}} \cdot \hat{k}|_{z=0}, \qquad (28)$$

where q is the full Ertel PV, the overline denotes a lateral av-erage, and primes denote a deviation from that average [*Tho-mas*, 2005]. At a fully three-dimensional front, an analogous result holds: along-isopycnal eddy PV fluxes on isopycnal surfaces that outcrop at a front that is forced with down-front winds scale with the frictional PV flux averaged over the outcrop window of the isopycnal (see Figure 5). Thus,

$$\int \int_{z=z_b}^{z=z_t} q''v'' \, dz \, dx \sim \int \int_{\mathcal{A}} \nabla_h b \times \mathbf{F} \cdot \hat{k}|_{z=0} \, dy \, dx \qquad (29)$$

where z_t, z_b are the top and bottom depths of the isopycnal layer, $\mathcal{A}$ is the area of the outcrop, x is the along-front direc-tion, and the double primes denote the deviation from the thickness-weighted isopycnal mean, i.e., $v'' = v - \overline{vh}^x/\overline{h}^x$, $h = z_t - z_b$ (the overline denotes a x average) [*Thomas*, 2007]. Results from a high-resolution numerical simulation demon-strating this are shown in Figure 5 to illustrate the correspond-ence between eddy and frictional PV fluxes. The details of the initial configuration and numerics of the simulation can be found in the work of *Thomas* [2007]. The key element of the experiment is that the front is initially aligned in the x di-
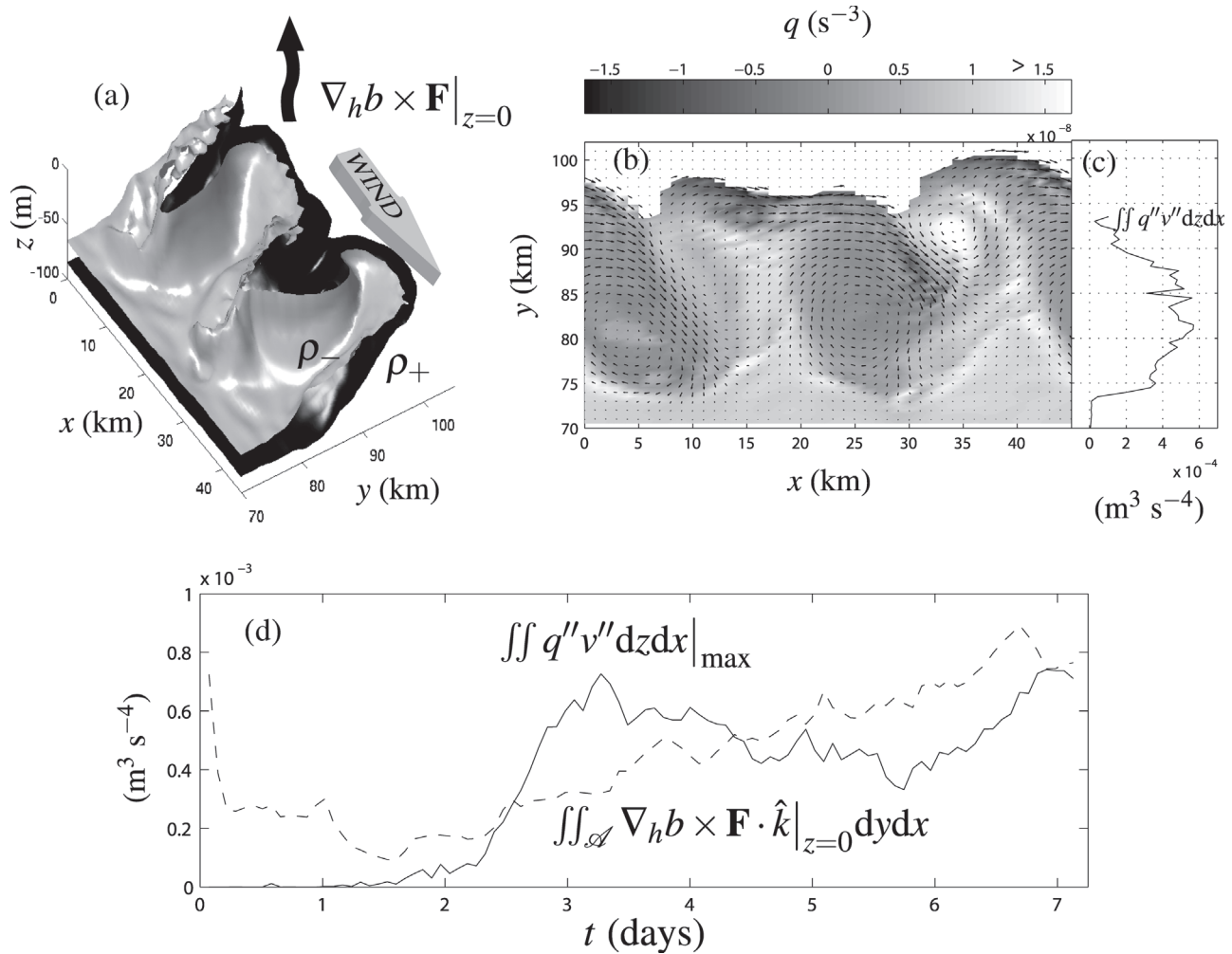
Figure 5. An example of submesoscale eddy PV fluxes driven by winds. (a) Down-front winds of strength 0.2 N m^{-2} forcing a front induce an upward frictional PV flux, triggering frontal instabilities that distort the bounding frontal isopycnal surfaces ρ_- (gray) and ρ_+ (black) ($\Delta\rho = \rho_+ - \rho_- = 0.2$ kg m^{-3}), shown here $t = 4.1$ days after the onset of the winds. (b) Isopycnal map of the PV (shades) and velocity (vectors) averaged in the vertical over the isopycnal layer shown in (a) illustrates the manner in which the instabilities subduct low PV from the surface while upwelling high PV from the pycnocline. (c) The correlation of the velocity and PV fields results in a net positive meridional eddy PV flux along the isopycnal layer $\iint q''v''dzdx > 0$. (d) A time series of the maximum value of the eddy PV flux with respect to y (solid) and the frictional PV flux integrated over the outcrop area (dashed) reveal that the two fluxes scale with one another after the initial growth of the instabilities, i.e. $t > 3$ days.

rection and is forced by a spatially uniform down-front wind that persists through the 7.3-day-long experiment (this differs from the experiment described by *Thomas* [2007] where the wind stress is shut off after 3.6 days). As can be seen in Figure 5b, the destruction of PV by the winds results in the formation of low, even negative, PV fluid where the frontal isopycnals outcrop into the surface Ekman layer ($z > -40$ m and 100 km $> y >$ 90 km). Streamers of low PV surface fluid are subducted into the interior by the submesoscale instabilities, while high PV interior fluid is drawn to the surface so

that a positive eddy PV flux is induced at the y locations of the eddies. Once the eddies grow to finite amplitude, the relation shown in (29) holds, Figure 5d. In an experiment where the winds are turned off, (29) also holds, but the eddy PV flux, which persists after the winds cease, scales with the frictional PV flux at the time of the wind forcing, suggesting that there is a temporally nonlocal relation between the two fluxes [*Thomas*, 2007].

Isopycnal eddy PV fluxes are important because they drive an eddy-induced transport velocity (also known as a

bolus velocity, which can be related to the residual circulation of the transformed Eulerian mean equations; *Plumb and Ferrari* [2005]) that can play an important role in the advection of tracers [*Greatbatch*, 1998]. When the tracer is the buoyancy, advection by the eddy transport velocity can result in restratification. Indeed, the process of mixed layer restratification by MLI described by Fox-Kemper et al. [2007] and summarized in section 4.1 is expressed in terms of the flattening of isopycnals by an overturning stream function associated with the residual circulation. In the wind-forced problem, the eddy transport velocity $v* = \overline{vh}^x/\overline{h} - \overline{v}^x$ was found to scale with the eddy PV flux, i.e., $v* \approx -\iint q''v''dzdx/(\Delta b L_x f)$, where Δb is the buoyancy difference across the isopycnal layer and L_x is the zonal width of the domain [*Thomas*, 2007]. As the eddy PV flux also scaled with the surface frictional PV flux, i.e., (29), and the magnitude of frictional force is set by the strength of the wind stress τ and Ekman depth δ_e, that is $|\mathbf{F}| \sim \tau/(\rho_o \delta_e)$, it was shown that the eddy transport velocity scaled with the Ekman flow $v_e \sim \tau/(\rho f \delta_e)$ [*Thomas*, 2007]. This result suggests that a closure scheme for submesoscale eddy PV fluxes and residual circulation at wind-forced baroclinic currents would have a

dependence on the wind stress, which would be in contrast to parameterizations based on down-gradient PV fluxes that make no explicit reference to atmospheric forcing.

4.3. Effect on Biogeochemistry

Submesoscales processes affect ocean biogeochemistry in multiple ways. First, as submesoscale vertical velocities are substantially higher than their mesoscale counterparts, the vertical fluxes they support enhance phytoplankton productivity and air-sea gas exchange. Phytoplankton productivity, and the strength of the biological pump, is typically limited by the availability of nutrients that are plentiful at depth, and light, which is at the surface. Modeling studies of fronts show that the upward flux of nutrients into the euphotic layer and consequently, new production, intensify with progressively higher horizontal model resolution (increased from 40 to 10 km by *Mahadevan and Archer* [2000] and from 6 to 2 km by *Lévy et al.* [2001]), signifying that submesoscale processes are at play. Second, as vertical motion is strongly linked to horizontal strain at submesoscales, regions of high strain in which tracer filaments are stretched and stirred by lateral motions at the surface


Domain-wide integrated consumption of nutrient-like tracer
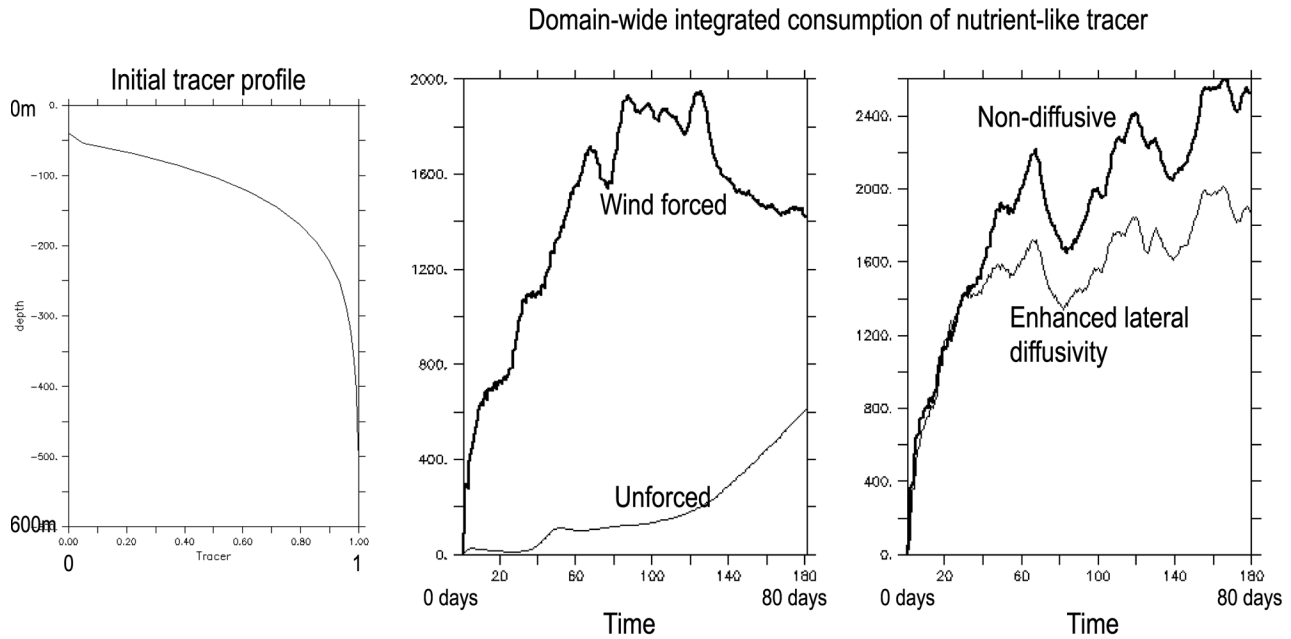
Figure 6. The domain-wide convergence of the vertical flux, or $\frac{1}{\tau}\overline{c'}|_{c'>0}$, which denotes the rate of nutrient uptake, is plotted as a function of time for two numerical experiments. In the middle panel, we compare the nutrient uptake rate for a model run that develops submesoscale structure due to a constant down-front wind, with one that is unforced and lacks submesoscale structure. In the right panel, we show another experiment where we compare the uptake rate between two cases: one in which the lateral diffusivity of the tracer is zero in the numerical model and a second in which it is enhanced to 100 m^2 s^{-1}. The lateral variability in the distribution of the tracer is shown in Figure 7. The left panel shows the initial tracer profile $c_0(z)$. In both experiments, the tracer concentrations are normalized between 0 and 1.

are also regions of intense up or downwelling. The vertical velocities, in turn, can affect the lateral stirring of a phytoplankton bloom and enhance phytoplankton productivity through nutrient supply in filaments as well as carbon export through the subduction of organic matter and the air-sea transfer of carbon dioxide. A further effect of submesoscale processes on ocean biogeochemistry is that they generate lateral gradients at scales of ~1 km and create spatial heterogeneity in property
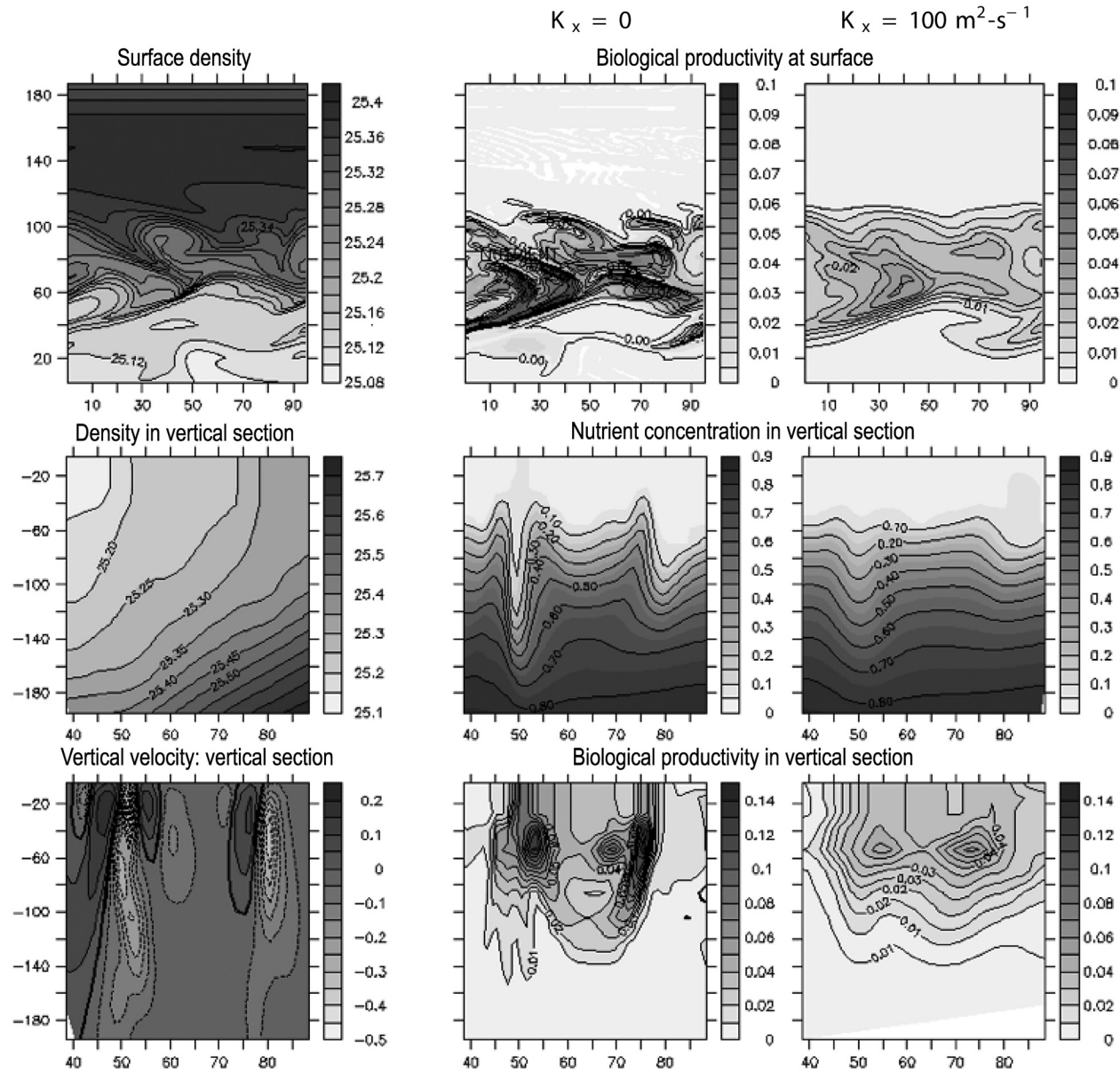
Figure 7. Modeling the nutrient and biological productivity due to submesoscale vertical fluxes shows a reduction in productivity when the lateral diffusivity of the biological tracers is increased to $100 \, \text{m}^2 \text{s}^{-1}$. The leftmost column shows the physical variables, density anomaly (in kg m^{-3}) and vertical velocity (in mm s^{-1}). These are the same for the two simulations compared. The middle column shows how the vertical submesoscale velocities supply nutrient and fuel biological productivity in the euphotic zone. The nutrient concentration is normalized between 0 and 1, and biological productivity is the rate of uptake of nutrient. The right column shows simulations with increased lateral diffusivity of the biogeochemical tracers. In this case, vertical nutrient transport is suppressed as pathways for transport are obliterated by diffusivity.

distributions. A number of biological processes are affected by distribution patchiness, as they are limited by access to nutrients, oxygen, or properties that are involved in a reaction.

Biogeochemical properties typically exhibit a large vertical concentration gradient because they are altered by processes that are depth-dependent but limited by the rate of vertical exchange. The ratio of the timescale of vertical advection to that of the processes altering the tracers (such as biological production) is an important parameter (termed the Damköhler number), which affects not only the biogeochemical tracer flux and the time-averaged vertical tracer profile but also the spatial heterogeneity of the tracer distribution in the upper ocean. Submesoscale processes increase lateral spatial heterogeneity of biogeochemical properties either by introducing submesoscale concentration anomalies due to vertical advection or by the lateral straining and drawing out of filaments. In the former case, an increase in the altering process (or reaction) timescale shifts the spatial variance towards larger scales [*Mahadevan and Campbell*, 2002]. In the latter, slower reaction timescales offer greater scope for filamentation and increased submsoscale spatial variance [*Abraham*, 1998].

We quantify the rate of vertical exchange in the upper ocean in numerical experiments by tracking the cumulative divergence of the vertical flux of a tracer c, with an initial vertical concentration profile $c_0(z)$. The profile $c_0(z)$ is chosen to represent the mean profile of a phytoplankton nutrient like nitrate; it is abundant at depth, but depleted from the surface, with a strong vertical gradient between 50 and 250 m (Figure 6). The rate of supply of the tracer for phytoplankton production, $-w\frac{\partial c}{\partial z}$, is the convergence of the vertical flux. Our numerical experiments are set within an east-west periodic domain, with a north-south density gradient representative of an upper ocean front. As the tracer is advected in the frontal flow field, we restore its concentration to the initial profile $c_0(z)$ with an e-folding timescale τ, such that

$$\frac{\partial c}{\partial t} + u\frac{\partial c}{\partial x} + v\frac{\partial c}{\partial y} + w\frac{\partial c}{\partial z} = -\frac{1}{\tau}\left(c - c_0(z)\right). \quad (30)$$

Faster restoring, that is smaller τ, maintains smaller values of $c - c_0(z)$, sharper vertical gradients, and thus higher vertical fluxes. When $c > c_0(z)$, the negative right-hand side term denotes the uptake of nutrient by phytoplankton. We quantify the convergence of vertical tracer flux over the entire domain by integrating the uptake of the nutrient-like tracer by phytoplankton. By writing $c = c_0(z) + c'$ and noting that the domain-wide average of c' (denoted by an overbar) is zero, that is $\overline{c'} = 0$, we get, for $\frac{\partial c}{\partial z} < 0$,

$$\overline{w^{(+)}\partial c/\partial z} = -\frac{1}{\tau}\overline{(c - c_0(z))}|_{c>c_0}, \quad (31)$$

where $w^{(+)}$ refers to positive (upward) w. Thus, the convergence of vertical flux, which is the rate of supply of nutrient, is calculated by evaluating the magnitude of the right hand side $\frac{1}{\tau}\overline{c'}\big|_{c'>0}$ of (31), specifically when $c' > 0$.

An enhancement of the rate of uptake of a nutrient-like tracer by wind-forced submesoscale instabilities can be seen in Figure 6 where we compare the vertical divergence of tracer flux from a numerical experiment in which submesoscale structure is generated by surface wind to a case without wind forcing and submesoscale structure. In these simulations, the mixed layer is 50 m deep. The tracer is restored to its initial profile $c_0(z)$ on a timescale $\tau = 3$ days. The convergence of vertical flux of tracer is the amount of tracer that is removed per time step to perform the described restoration of the tracer profile. By treating the tracers identically in both the wind-forced and unforced cases, the difference in the nutrient uptake can be attributed entirely to the differences in the vertical velocities between the model runs, which turns out to be substantial.

In another experiment (Figure 7), the lateral variability in tracer distribution introduced by submesoscale processes is suppressed by increasing the lateral diffusivity of the tracer. The result is that narrow pathways for vertical transport are obliterated, and vertical tracer flux is substantially diminished (Figure 6, right panel). When the tracer is considered to be nitrate and its vertical transport results in phytoplankton productivity, the lateral diffusion of tracer diminishes phytoplankton productivity in the model.

5. DISCUSSION

As described in section 4.1, restratification of the mixed layer by submesoscale flows is accomplished at the expense of the available potential energy (APE) stored in the larger scale baroclinic currents in which they form. This characteristic of submesoscale flows, which is a consequence of their strong secondary circulations, hints at their potentially important role in the energy budget of the ocean, a subject that is explored in this section.

The power spectrum of kinetic energy is often used to characterize the energy distribution in terms of lengthscales. While three-dimensional turbulence spectra show a characteristic $-5/3$ power law (or $-5/3$ slope in log-log space) and the cascade of energy to smaller scales, stratified quasi-geostrophic mesoscale flow (geostrophic turbulence) spectra have a -3 slope [e.g., *Vallis*, 2006] and a

reverse energy cascade. With increasing grid resolution in a primitive equation model, *Capet et al.* [2008a] find the spectral slope transitions from −3 at mesoscale resolutions to −2 at submesoscales in the upper ocean (also seen in *Legg and McWilliams* [2001]). *Boccaletti et al.* [2007] and *Fox-Kemper et al.* [2007] show that the energy peak triggered by mixed layer instability is transferred to both larger and smaller scales. The reverse cascade is physically manifest through the evolution of mixed layer eddies into larger ones, while the forward cascade is intimately tied to frontogenesis and frontal instabilities.

Finite depth surface quasi-geostrophic (SQG) models have been used to explain the transition from −3 to −5/3 slope in atmospheric spectra derived from aircraft observations [*Tulloch and Smith*, 2006]. SQG has also been advanced by *Lapeyre et al.* [2006] as appropriate for $O(1)$ Rossby number flows with scales smaller than mesoscales. For the oceanic case, simulations by *Klein et al.* [2007] show a transition from −3 to −5/3 slope in the EKE spectrum from the interior to the upper ocean, with a reverse cascade at larger scales and a forward energy cascade at $O(1)$ km. As shown in section 3.1.2, the frontogenetic motion described by semi-geostrophic equations also produces a forward energy cascade, as smaller lengthscale structures arise as frontogenesis occurs. In contrast to the QG equations, the SG equations do not neglect advection by ageostrophic flow. (Capet et al., Mesoscale to submesoscale transition in the California Current System: Energy balance and flux, submitted to *Journal of Physical Oceanography*, 2007) show that although their contribution to the eddy kinetic energy (EKE) is small, the forward kinetic energy (KE) flux is entirely associated with advection by the horizontally divergent, ageostrophic component of the flow. Although the ageostrophic flow is weaker than the geostrophic flow, it plays a critical role in the forward cascade at small scales and in frontogenesis (Molemaker et al., Balanced and unbalanced routes to dissipation in an equilibrated Eady flow, submitted to *Journal of Fluid Mechanics*, 2007). It also follows that the vertical velocity distribution in the SQG and SG models is different and will likely result in very different vertical tracer fluxes. The SQG^{+1} extension model of *Hakim et al.* [2002] allows for cyclonic/anticyclonic asymmetry and an up/down asymmetry in the vertical velocity similar to the SG model because both include higher order contributions to the potential vorticity.

As discussed in section 3.1.2 and by *Andrews and Hoskins* [1978], the semigeostrophic frontal equation leads to flattening of the slope of the KE spectrum to −8/3 at the time of frontal collapse. *Boyd* [1992] shows that this slope is ephemeral, and as the front evolves into a discontinuity, the slope of the energy spectra would flatten further to −2, which is characteristic of jump discontinuities. Numerical experiments that are actively being forced, either by buoyancy loss [*Legg and McWilliams*, 2001] or by wind stress [*Capet et al.*, 2008a], also show a −2 slope for EKE, raising questions about the relative contributions of atmospheric forcing, frontogenesis, and APE release by instability in the energetics of submesoscale flows.

Many questions remain open with regard to submesoscales. The numerical experiments described in section 4.2 emphasized the role of wind forcing in driving submesoscale eddy PV fluxes. It remains to be seen if a similar result holds true for submesoscale motions driven by atmospheric buoyancy fluxes. Another question is whether there is a general relation between nonadvective PV fluxes (frictional or diabatic) induced by atmospheric forcing and eddy PV fluxes or whether the relation is specific to the case of down-front winds.

The cumulative effects of submesoscale processes on larger scales are beginning to be assessed in terms of mixed layer restratification (B. Fox-Kemper and R. Ferrari, Parameterization of mixed layer restratification. II: Prognosis and impact, submitted to *Journal of Physical Oceanography*, 2007), although it is not well understood how submesoscale dynamics affect the PV budget at the large scale. A review of the general ocean circulation energetics by *Wunsch and Ferrari* [2004] notes that the energy pathways from mesoscale eddies to internal waves are not well understood and have not been quantified. As it turns out that the limits of balance coincide with the growth of unbalanced instabilities at the submesoscale, it is possible that the energy pathway from mesoscale to internal waves is via unbalanced submesoscale instabilities [*Molemaker et al.*, 2005]. However, it remains to be shown whether this breakdown in balance leads to triggering energy into internal gravity waves or whether direct interactions between the balanced submesoscale flows and a preexisting internal wave field affects energy transfer from large to small scales [*Bühler and McIntyre*, 2005; K. L. Polzin, How Rossby waves break. Results from POLYMODE and the end of the enstrophy cascade, submitted to *Journal of Physical Oceanography*, 2006]. Whatever the mechanism, the downscale cascade of energy from submesoscales could have far-reaching implications on mixing and dissipation. This, plus the implications for vertical transport of buoyancy, momentum, and biogeochemical properties, makes it important to improve our understanding of submesoscale phenomena.

REFERENCES

Abraham, E. R. (1998), The generation of plankton patchiness by turbulent stirring, *Nature*, *391*, 577–580.

Allen, J. T., and D. Smeed (1996), Potential vorticity and vertical velocity at the Iceland-Faroes front, *J. Phys. Oceanogr.*, *26*, 2611–2634.

Andrews, D. G., and B. J. Hoskins (1978), Energy spectra predicted by semi-geostrophic theories of frontogenesis, *J. Atmos. Sci.*, *35*, 509–512.

Boccaletti, G., R. Ferrari, and B. Fox-Kemper (2007), Mixed layer instabilities and restratification, *J. Phys. Oceanogr.*, *37*, 2228–2250.

Boyd, J. P. (1992), The energy spectrum of fronts: Time evolution of shocks in Burgers' equation, *J. Atmos. Sci.*, *49*, 128–139.

Bühler, O., and M. E. McIntyre (2005), Wave capture and wave-vortex duality, *J. Fluid Mech.*, *534*, 67–95.

Capet, X., J. C. McWilliams, M. J. Molemaker, and A. F. Shchepetkin (in press), Mesoscale to submesoscale transition in the California Current System: Flow structure, eddy flux, and observational tests, *J. Phys. Oceanogr.*

Capet, X., J. C. McWilliams, M. J. Molemaker, and A. F. Shchepetkin (in press), Mesoscale to submesoscale transition in the California Current System: Frontal processes, *J. Phys. Oceanogr.*

Charney, J. G. (1948), On the scale of atmospheric motions, *Geosphys. Publ. Oslo*, *17*(2), 1–17.

Charney, J. G. (1971), Geostrophic turbulence, *J. Atmos. Sci.*, *28*, 1087–1095.

Eliassen, A. (1948), The quasi-static equations of motion, *Geofys. Publikasjoner*, *17* (3).

Eliassen, A. (1951), Slow thermally or frictionally controlled meridional circulation in a circular vortex, *Astrophys. Norv.*, *5*, 19–60.

Emerson, S., P. Quay, D. Karl, C. Winn, L. Tupas, and M. Landry (1997), Experimental determination of the organic carbon flux from open-ocean surface waters, *Nature*, *389*, 951–954.

Flament, P., L. Armi, and L. Washburn (1985), The evolving structure of an upwelling filament, *J. Geophys. Res.*, *90*, 11,765–11,778.

Fox-Kemper, B., R. Ferrari, and R. Hallberg (in press), Parameterization of mixed layer restratification. I: Theory and validation, *J. Phys. Oceanogr.*

Gent, P. R., and J. C. McWilliams (1983), Consistent balanced models in bounded and periodic domains, *Dyn. Atmos. Oceans*, *7*, 67–93.

Gent, P. R., J. C. McWilliams, and C. Snyder (1994), Scaling analysis of curved fronts: validity of the balance equations and semigeostrophy, *J. Atmos. Sci.*, *51*, 160–163.

Greatbatch, R. J. (1998), Exploring the relationship between eddy-induced transport velocity, vertical momentum transfer, and the isopycnal flux of potential vorticity, *J. Phys. Oceanogr.*, *28*, 422–432.

Haine, T. W. N., and J. C. Marshall (1998), Gravitational, symmetric, and baroclinic instability of the ocean mixed layer, *J. Phys. Oceanogr.*, *28*, 634–658.

Hakim, G. J., and D. Keyser (2001), Canonical frontal circulation patterns in terms of Green's functions for the Sawyer-Eliassen equation, *Q. J. R. Meteorol. Soc.*, *127*, 1795–1814.

Hakim, G. J., C. Snyder, and D. J. Muraki (2002), A new surface model for cyclone–anticyclone asymmetry, *J. Atmos. Sci.*, *59*, 2405–2420.

Hallberg, R. (2003), The suitability of large-scale ocean models for adapting parameterizations of boundary mixing and a description of a refined bulk mixed layer model, in *Proceedings of the 2003 'Aha Huliko'a Hawaiian Winter Workshop*, University of Hawaii, pp. 187–203.

Hoskins, B. J. (1975), The geostrophic momentum approximation and the semi-geostrophic equations, *J. Atmos. Sci.*, *32*, 233–242.

Hoskins, B. J., and F. P. Bretherton (1972), Atmospheric frontogenesis models: Mathematical formulation and solution, *J. Atmos. Sci.*, *29*, 11–37.

Hoskins, B. J., and I. Draghici (1977), The forcing of ageostrophic motion according to the semi-geostrophic equations and in an isentropic coordinate model, *J. Atmos. Sci.*, *34*, 1859–1867.

Hoskins, B. J., I. Draghici, and H. C. Davies (1978), A new look at the ω-equation., *Q. J. R. Meteorol. Soc.*, *104*, 31–38.

Jenkins, W. J. (1988), Nitrate flux into the euphotic zone near Bermuda, *Nature*, *331*, 521–523.

Jenkins, W. J., and J. C. Goldman (1985), Seasonal oxygen cycling and primary production in the Sargasso Sea, *J. Mar. Res.*, *43*, 465–491.

Klein P., B. L. Hua, G. Lapeyre, X. Capet, S. Le Gentil, and H. Sasaki (in press), Upper ocean turbulence from high 3-D resolution simulations, *J. Phys. Oceanogr.*

Kunze, E. (2001), Vortical modes, in *Encyclopedia of Ocean Sciences*, edited by S. T. J. Steele and K. Turekian, pp. 3174–3178, Academic, London.

Kunze, E., and T. B. Stanford (1993), Submesoscale dynamics near a seamount, *J. Phys. Oceanogr.*, *23*, 2567–2601.

Lapeyre, G., P. Klein, and B. L. Hua (2006), Oceanic restratification forced by surface frontogenesis, *J. Phys. Oceanogr.*, *36*, 1577–1590.

Lee, C. M., E. A. D'Asaro, and R. Harcourt (2006a), Mixed layer restratification: Early results from the AESOP program, *Eos Trans. AGU, 87*(52)*, Fall Meet. Suppl., Abstract OS51E-04*.

Lee, C. M., L. N. Thomas, and Y. Yoshikawa (2006b), Intermediate water formation at the Japan/East Sea subpolar front, *Oceanography*, *19*, 110–121.

Legg, S., and J. C. McWilliams (2001), Convective modifications of a geostrophic eddy field, *J. Phys. Oceanogr.*, *31*, 874–891.

Legg, S., J. C. McWilliams, and J. Gao (1998), Localization of deep ocean convection by a mesoscale eddy, *J. Phys. Oceanogr.*, *28*, 944–970.

Lévy, M., P. Klein, and A. M. Treguier (2001), Impacts of submesoscale physics on production and subduction of phytoplankton in an oligotrophic regime, *J. Mar. Res.*, *59*, 535–565.

Mahadevan, A. (2006), Modeling vertical motion at ocean fronts:

Are nonhydrostatic effects relevant at submesoscales?, *Ocean Model.*, *14*, 222–240.

Mahadevan, A., and D. Archer (2000), Modeling the impact of fronts and mesoscale circulation on the nutrient supply and biogeochemistry of the upper ocean, *J. Geophys. Res.*, *105* (C1), 1209–1225.

Mahadevan, A., and J. W. Campbell (2002), Biogeochemical patchiness at the sea surface, *Geophys. Res. Lett.*, *29* (19), 1926, doi:10.10292001GL014116.

Mahadevan, A., and A. Tandon (2006), An analysis of mechanisms for submesoscale vertical motion at ocean fronts, *Ocean Model.*, *14 (3-4)*, 241–256.

Maier-Reimer, E. (1993), Geochemical cycles in an ocean general circulation model, *Global Biogeochem. Cycles*, *7*, 645–678.

Marshall, J. C., and A. J. G. Nurser (1992), Fluid dynamics of oceanic thermocline ventilation., *J. Phys. Oceanogr.*, *22*, 583–595.

Martin, A. P., and P. Pondaven (2003), On estimates for the vertical nitrate flux due to eddy-pumping, *J. Geophys. Res.*, *108* (C11), 3359, doi: 10.1029/2003JC001841.

McGillicuddy, D. J., Jr., and A. R. Robinson (1997), Eddy induced nutrient supply and new production in the Sargasso Sea, *Deep-Sea Res.*, *44* (8), 1427–1450.

McGillicuddy, D. J., Jr., A. R. Robinson, D. A. Siegel, H. W. Jannasch, R. Johnson, T. D. Dickey, J. McNeil, A. F. Michaels, and A. H. Knap (1998), Influence of mesoscale eddies on new production in the Sargasso Sea, *Nature*, *394*, 263–266.

McKiver, W. J., and D. G. Dritschel (2008), Balance in non-hydrostatic rotating stratified turbulence, *J. Fluid Mech.*, *596*, 201–219.

McWilliams, J. C. (1985), Submesoscale, coherent vortices in the ocean, *Rev. Geophys.*, *23*, 165–182.

McWilliams, J. C. (2003), Diagnostic force balance and its limits, in *Nonlinear Processes in Geophysical Fluid Dynamics*, edited by O. V. Fuentes, J. Sheinbaum, and J. Ochoa, pp. 287–304, Kluwer, Dordrecht.

McWilliams, J. C., and P. R. Gent (1980), Intermediate models of planetary circulations in the atmosphere and ocean, *J. Atmos. Sci.*, *37*, 1657–1678.

McWilliams, J. C., M. J. Molemaker, and I. Yavneh (2001), From stirring to mixing of momentum: Cascades from balanced flows to dissipation, in *Proceedings of the 12th 'Aha Huliko'a Hawaiian Winter Workshop*, University of Hawaii, pp. 59–66.

Molemaker, M. J., J. C. McWilliams, and I. Yavneh (2005), Baroclinic instability and loss of balance, *J. Phys. Oceanogr.*, *35*, 1505–1517.

Munk, W., L. Armi, K. Fischer, and F. Zachariasen (2000), Spirals on the sea, *Proc. R. Soc. Lond. A*, *456*, 1217–1280.

Nagai, T., A. Tandon, and D. L. Rudnick (2006), Two-dimensional ageostrophic secondary circulation at ocean fronts due to vertical mixing and large-scale deformation, *J. Geophys. Res.*, *111*, C09038, doi:10.1029/2005JC002964.

Najjar, R. G., J. L. Sarmiento, and J. R. Toggweiler (1992), Downward transport and fate of organic matter in the ocean: Simulations with a general circulation model, *Global Biogeochem. Cycles*, *6*, 45–76.

Naveira Garabato, A. C., J. T. Allen, H. Leach, V. H. Strass, and R.

T. Pollard (2001), Mesoscale subduction at the Antarctic Polar Front driven by baroclinic instability, *J. Phys. Oceanogr.*, *31*, 2087–2107.

Niiler, P. P. (1969), On the Ekman divergence in an oceanic jet, *J. Geophys. Res.*, *74*, 7048–7052.

Oschlies, A. (2002a), Can eddies make ocean deserts bloom?, *Glob. Biogeochem. Cycles*, *16*, 1106, doi:10.1029/2001GB001830.

Oschlies, A. (2002b), Improved representation of upper-ocean dynamics and mixed layer depths in a model of the North Atlantic on switching from eddy-permitting to eddy-resolving grid resolution, *J. Phys. Oceanogr.*, *32*, 2277–2298.

Oschlies, A. (2007), Eddies and upper ocean nutrient supply, this volume.

Pallàs Sanz, E., and A. Viúdez (2005), Diagnosing mesoscale vertical motion from horizontal velocity and density data, *J. Phys. Oceanogr.*, *35*, 1744–1762.

Pinot, J. M., J. Tintoré, and D. P. Wang (1996), A study of the omega equation for diagnosing vertical motions at ocean fronts, *J. Mar. Res.*, *54*, 239–259.

Platt, T., and W. G. Harrison (1985), Biogenic fluxes of carbon and oxygen in the ocean, *Nature*, *318*, 55–58.

Plumb, R. A., and R. Ferrari (2005), Transformed Eulerian-mean theory. Part I: Nonquasigeostrophic theory for eddies on a zonal-mean flow, *J. Phys. Oceanogr.*, *35*, 165–174.

Pollard, R. T., and L. Regier (1992), Vorticity and vertical circulation at an ocean front, *J. Phys. Oceanogr.*, *22*, 609–625.

Polzin, K. L., and R. Ferrari (2003), Isopycnal dispersion in NATRE, *J. Phys. Oceanogr.*, *34*, 247–257.

Rudnick, D. L. (1996), Intensive surveys of the Azores front. Inferring the geostrophic and vertical velocity fields, *J. Geophys. Res.*, *101* (C7), 16,291–16,303.

Rudnick, D. L. (2001), On the skewness of vorticity in the upper ocean, *Geophys. Res. Lett.*, *28*, 2045–2048.

Rudnick, D. L., and J. R. Luyten (1996), Intensive surveys of the Azores front 2. Tracers and dynamics, *J. Geophys. Res.*, *101*, 923–939.

Rudnick, D., L. and R. Ferrari (1999), Compensation of horizontal temperature and salinity gradients in the ocean mixed layer, *Science*, *283*, 526–529.

Sawyer, J. S. (1956), The vertical circulation at meteorological fronts and its relation to frontogenesis, *Proc. R. Soc. Lond. A*, *234*, 346–362.

Shay, L. K., T. M. Cook, and P. E. An (2003), Submesoscale coastal ocean flows detected by very high frequency radar and autonomous underwater vehicles, *J. Atmos. Oceanic Technol.*, *20*, 1583–1599.

Shearman, R. K., J. M. Barth, and P. M. Kosro (1999), Diagnosis of three-dimensional circulation associated with mesoscale motion in the California current, *J. Phys. Oceanogr.*, *29*, 651–670.

Stern, M. E. (1965), Interaction of a uniform wind stress with a geostrophic vortex., *Deep-Sea Res.*, *12*, 355–367.

Stone, P. H. (1966), On non-geostrophic baroclinic stability, *J. Atmos. Sci.*, *23*, 390–400.

Stone, P. H. (1970), On non-geostrophic baroclinic stability: Part II, *J. Atmos. Sci.*, *27*, 721–727.

Stone, P. H. (1971), Baroclinic instability under non-hydrostatic conditions, *J. Fluid Mech.*, *45*, 659–671.

Sundermeyer, M. A., and M. P. Lelong (2005), Numerical simulations of lateral dispersion by the relaxation of diapycnal mixing events, *J. Phys. Oceanogr.*, *35*, 2368–2386.

Tandon, A., and C. Garrett (1994), Mixed layer restratification due to a horizontal density gradient, *J. Phys. Oceanogr.*, *24*, 1419–1424.

Thomas, L. N. (2005), Destruction of potential vorticity by winds, *J. Phys. Oceanogr.*, *35*, 2457–2466.

Thomas, L. N. (2007), Formation of intrathermocline eddies at ocean fronts by wind-driven destruction of potential vorticity, *Dyn. Atmos. Oceans*, accepted.

Thomas, L. N., and C. M. Lee (2005), Intensification of ocean fronts by down-front winds, *J. Phys. Oceanogr.*, *35*, 1086–1102.

Thomas, L. N., and P. B. Rhines (2002), Nonlinear stratified spin-up, *J. Fluid Mech.*, *473*, 211–244.

Tulloch, R., and K. S. Smith (2006), A theory for the atmospheric energy spectrum: Depth limited temperature anomalies at the tropopause, *Proc. Natl. Acad. Sci. U.S.A.*, *103* (40), 14,690–14,694.

Vallis, G. K. (2006), *Atmospheric and Oceanic Fluid Dynamics: Fundamentals and Large-scale Circulation*, 745 pp., Cambridge University Press, Cambridge.

Vélez-Belchí, P., M. Vargas-Yáñez, and J. Tintoré (2005), Observation of a western Alborán gyre migration event, *Prog. Oceanogr.*, *66*, 190–210.

Viúdez, A. (2005), The vorticity-velocity gradient cofactor tensor and the material invariant of the semigeostrophic theory, *J. Phys. Oceanogr.*, *62*, 2294–2301.

Viúdez, A., and D. G. Dritschel (2004), Optimal potential vorticity balance of geophysical flows, *J. Fluid Mech.*, *521*, 343–352.

Viúdez, A., J. Tintoré, and R. Haney (1996), Circulation in the Alborán Sea as determined by quasi-synoptic hydrographic observations. Part I: Three-dimensional structures of the two anticyclonic gyres, *J. Phys. Oceanogr.*, *26*, 684–705.

Waite, M. L., and P. Bartello (2006), The transition from geostrophic to stratified turbulence, *J. Fluid Mech.*, *568*, 89–108.

Wunsch, C., and R. Ferrari (2004), Vertical mixing, energy and the general circulation of the oceans, *Annu. Rev. Fluid Mech.*, *36*, 281–314.

Yoshikawa, Y., K. Akitomo, and T. Awaji (2001), Formation process of intermediate water in baroclinic current under cooling, *J. Geophys. Res.*, *106*, 1033–1051.

_____

Amala Madevan, Department of Earth Sciences, Boston University, 685 Commonwealth Avenue, Boston, MA 02215, USA. (amala@bu.edu)

Amit Tandon, Physics Department and Department of Estuarine and Ocean Sciences, University of Massachusetts, Dartmouth, 285 Old Westport Road, North Dartmouth, MA 02747, USA. (atandon@umassd.edu)

Leif N. Thomas, Department of Physical Oceanography, Woods Hole Oceanographic Institution, MS 21, Woods Hole, MA 02543, USA. (lthomas@whoi.edu)